

Behavioral Signatures of a Developing Neural Code

Highlights

- Development of zebrafish hunting behavior and tectal activity
- Hunting behavior becomes more efficient and accurate over development
- Neural decoding and information transmission improve over development
- Individual differences in decoding predict hunting performance

Authors

Lilach Avitan, Zac Pujic, Jan Mölter, ..., Biao Sun, Ann-Elin Myhre, Geoffrey J. Goodhill

Correspondence

g.goodhill@uq.edu.au

In Brief

How do neural codes critical for behavior emerge during development? Avitan et al. show that during early life, visually driven hunting in larval zebrafish improves, and this is accompanied by increasing mutual information and improved decoding of visual stimuli in the optic tectum. Moreover, decoding can predict individual differences in hunting.



Article

Behavioral Signatures of a Developing Neural Code

Lilach Avitan,^{1,3} Zac Pujic,¹ Jan Mölter,^{1,2} Michael McCullough,¹ Shuyu Zhu,¹ Biao Sun,¹ Ann-Elin Myhre,¹ and Geoffrey J. Goodhill^{1,2,4,*}

¹Queensland Brain Institute, The University of Queensland, Brisbane, Queensland 4072, Australia

²School of Mathematics and Physics, The University of Queensland, Brisbane, Queensland 4072, Australia

³Present address: Edmond & Lily Safra Center for Brain Sciences, Hebrew University, Jerusalem 9190401, Israel

⁴Lead Contact

*Correspondence: g.goodhill@uq.edu.au

<https://doi.org/10.1016/j.cub.2020.06.040>

SUMMARY

During early life, neural codes must develop to appropriately transform sensory inputs into behavioral outputs. Here, we demonstrate a link between the maturity of neural coding in the visual brain and developmental changes in visually guided behavior. In zebrafish larvae, we show that visually driven hunting behavior improves from 4 to 15 days post-fertilization, becoming faster and more accurate. During the same period, population activity in parts of the optic tectum refines, improving decoding and information transmission for particular spatial positions. Remarkably, individual differences in decoding can predict each fish's hunting success. Together, these results help reveal how the neural codes required for a natural behavior emerge during development.

INTRODUCTION

During early development, the brain must build neural codes appropriate for survival [1]. Techniques like fluorescent calcium imaging for recording the activity of many neurons simultaneously have recently facilitated new insights into the development of neural coding. In the mammalian cortex in particular, knowledge is expanding rapidly regarding the development of neural circuits [2–5]. However, the behavioral repertoire in the neonatal period of most of the mammalian species studied in this regard is relatively limited [6]. Therefore, the impact of these early developmental changes in neural coding on measurable aspects of behavior remains largely unknown.

In contrast, zebrafish larvae display sophisticated natural behaviors from only a few days post-fertilization (dpf). Retinal ganglion cell axons reach the optic tectum (the main visual processing center in zebrafish, homologous to the superior colliculus in mammals) from 2 dpf [7, 8], and from 5 dpf, the visuomotor system is already mature enough for larvae to hunt moving prey such as *Paramecia* [9–11]. A hunting event proceeds via a series of stereotyped bouts of movement driven by sequentially refined localization of the prey in visual space [12, 13]. An algorithmic description of larval zebrafish hunting has yet to be established, but recent evidence suggests that the sequence of actions during an event is driven by factors like the relative position and velocity of prey, the previous bout type, and hunger [14–16]. As zebrafish approach maturity, hunting behavior refines from bouts to much smoother movement [17]; however, how it changes over the first few days of hunting experience remains relatively uncharacterized. During this period, it is possible to image the activity of large populations of neurons in the zebrafish brain using fluorescent calcium indicators. Spontaneous activity in the optic tectum over this time follows a specific developmental trajectory, with an increased overall activity at the single-cell level, increased synchronous activity, and an

increase in measures of functional connectivity at 5 dpf, which then refines at 7–9 dpf [18, 19]. This activity also exhibits spatial patterns that match behaviorally relevant evoked patterns [20]. Tectal activity induced by visual cues can be used to decode the spatial position of prey-like spots [21]. However, whether the quality of this decoding changes with age, and how these developing neural properties are related to changes in behavior, remains unknown.

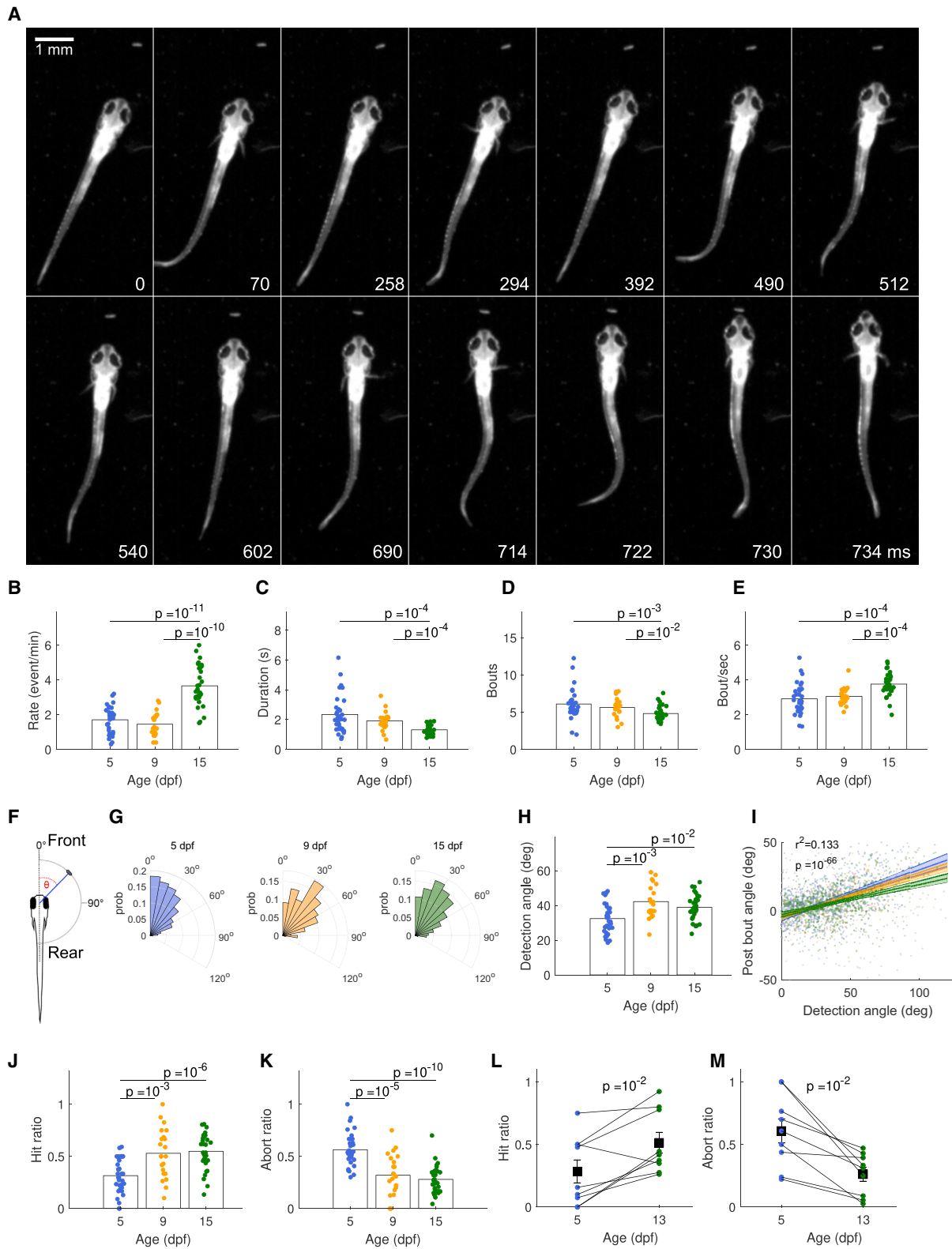
Here, we show that there is a systematic refinement in hunting behavior over the first few days when zebrafish larvae begin to hunt prey and that this is correlated with a systematic improvement in the quality of decoding and information transmission of spatial position in a part of the optic tectum. The latter improvement follows a specific spatiotemporal trajectory, suggestive of a changing balance of priority between predator avoidance and prey capture. Furthermore, the hunting success of individual fish can be predicted from the quality of neural coding in this part of the tectum. Together, this work addresses how developmental changes in behavior can be related to developmental changes in neural coding.

RESULTS

Hunting Performance Improves over Development

To study the development of a natural behavior, we imaged larval zebrafish hunting *Paramecia* at 5, 8–9, and 13–15 dpf ($n = 34, 22,$ and 33 , fish respectively, different fish for each age; for brevity, we hereafter refer to the older groups as simply 9 dpf and 15 dpf, respectively). Zebrafish transition from self-feeding via the yolk sac to feeding via hunting behavior at 5 dpf [22]. A hunting event commences with eye convergence, typically concurrent with a stereotyped turn bout toward the prey known as a J-turn [23]. Larvae then maintain their eyes in a highly converged position through a series of approach swims until they strike at the prey or abort the hunt [11, 23, 24, 25].





(legend on next page)

Each larva was placed in a dish with 30–50 *Paramecia* and behavior was imaged for 15–25 min using a high-speed camera. A typical hunting event is shown in Figure 1A. We analyzed all hunting events per fish and examined their developmental trajectory (see STAR Methods). Hunting event rate, i.e., the number of events per minute, increased over development (Figure 1B; unless otherwise stated, in all figures, each point represents the mean value for one fish over all events). Hunting events in which the fish performed a strike became shorter in duration (Figure 1C). Distance to the prey at the onset of the event did not change over development (Figure S1A). Hunting events consisted of fewer bouts with age (Figure 1D), and within the event, bout rate increased (Figure 1E), suggesting that larvae become more efficient at executing this behavior. Since individual fish can develop at different rates, we also examined these measures as a function of length in addition to age (Figure S1B), and all trends were preserved (Figures S1C–S1F).

We defined the time of prey detection as the onset of the hunting event marked by eye convergence. In each event, the *Paramecium* of interest was defined as the nearest *Paramecium* toward which the fish performed the first turn movement. To examine the spatial relationship between the larva and the *Paramecium* of interest, at the time of prey detection, we calculated the angle between them at the frame prior to eye convergence (Figure 1F) (see STAR Methods). These angles were predominantly in the frontal visual field, i.e., angles <90 degrees (Figure 1G), with a slight increase in angle in older fish (Figures 1H and S1G). The first bout tended to undershoot the angle required to align the fish with the prey, but this undershoot became smaller with age (Figure 1I). By calculating a handedness measure $(R - L)/(R + L)$, where R and L are the number of detections by the right and left eye respectively, we found no lateralization in *Paramecia* position at the time of prey detection (Figures S1H and S1I).

A hunting event was labeled as a hit event if the fish struck accurately at the *Paramecium* of interest, a miss event if the fish struck inaccurately and missed the prey, and an abort event

if the fish pursued the *Paramecium* of interest but aborted the pursuit and never struck at the prey (see STAR Methods). The hit ratio, i.e., the fraction of hit events out of all hunting events recorded per fish, increased over development (Figures 1J and S1J). This could be largely explained by a decrease in abort ratio, the fraction of abort events out of all hunting events recorded per fish over development (Figures 1K, S1K, and S1L).

For the results so far, each fish was only evaluated at one age. For a smaller number of fish ($n = 9$), we performed the more challenging experiment of evaluating hunting performance in the same fish at both 5 and 13 dpf (see STAR Methods). For 8 of 9 fish, the hit ratio improved (Figure 1L), and for all fish, the abort ratio decreased (Figure 1M). Other measures of performance also increased (Figures S1M–S1P), demonstrating that improvement at the group level was reflected in improvement in individual fish. Thus, although hunting behavior is often considered to be highly stereotyped, its characteristics change substantially over early development, with more efficient execution of hunting events and improved hunting performance.

Changes in Neural Responses over Development

We next asked whether these developmental changes in hunting behavior are correlated with developmental changes in the neural representation of the visual world. We embedded 4-, 5-, 8–9-, and 13–15-dpf *elavl3:H2B-GCaMP6s* fish ($n = 11, 17, 10,$ and 7 fish, respectively, different fish for each age, and as before, the older groups are referred to as 9 dpf and 15 dpf, respectively) in agarose for 2-photon calcium imaging of the optic tectum, a structure essential for hunting behavior [26] (see STAR Methods). Of these, 17 fish had previously been imaged for behavior and are included in Figure 1. First, we recorded from a depth of 70 μm below the surface of the skin, similar to the depth studied in some previous work [18]. We recorded 61.6 min of evoked activity in response to twenty repetitions of nine 6' diameter stationary spots (a size likely to be interpreted as prey [23]). Spots were presented for 1 s each with a 20 s gap between spots (to allow the GCaMP activity to completely decay), with a total of

Figure 1. Hunting Performance Improves over Development

- (A) A sequence of frames during a hunting event from the moment of prey detection (0 ms), showing orientation and eye convergence (70 ms), approach (294, 512 ms), strike (714–730 ms), and prey capture (734 ms).
- (B) Hunting event rate is higher for 15-dpf than for 5- and 9-dpf fish (t test).
- (C) Hunting events become shorter over development (Wilcoxon rank-sum).
- (D) Number of bouts per event is lower for 15-dpf than for 9- and 5-dpf fish (Wilcoxon rank-sum)..
- (E) Bout rate is higher at 15 dpf than at 5 and 9 dpf (t test).
- (F) Detection angle is defined as the angle between a *Paramecium* and the midline of the fish just prior to eye convergence.
- (G) Distributions of prey detection angle for 5-, 9-, and 15-dpf fish change over development (5 versus 9, $p = 10^{-7}$; 5 versus 15, $p = 10^{-6}$; 9 versus 15, $p = 0.05$; two-sample Kolmogorov-Smirnov test).
- (H) 9- and 15-dpf fish detect *Paramecia* at larger angles (i.e., toward the rear visual field) than do 5-dpf fish.
- (I) The relation between prey detection angle and angle to prey after the first bout (here, each point represents a bout rather than a fish). Multiple regression analysis (see STAR Methods) reveals a positive correlation between detection angle and post-bout angle, indicating that the fish undershoot the turn (coefficient $\beta_1 = 0.417$; $p = 10^{-22}$) and that the degree of undershoot reduces with age (coefficient $\beta_3 = -0.013$; $p = 10^{-3}$). Turn angle does not change with age independently of prey angle ($\beta_2 = 0.25$; $p = 0.08$). Solid lines show the fitted regression model for each age. Shaded regions show the 95% confidence intervals for each slope. r^2 statistic and p value shown are for the overall model. For clarity, the small number of turns falling outside the range between -50 and 50 degrees are not plotted.
- (J) Hunting performance, as measured by the proportion of all hunting events per fish which are successful, increases over development (t test).
- (K) Abort ratio decreases over development (t test).
- (L) Hunting performance of individuals imaged at both 5 and later at 13 dpf increases over development (paired-sample t test). Black squares represent the mean; bars, SEMs.
- (M) Abort ratio of individuals imaged at both 5 and later at 13 dpf decreases over development (paired-sample t test). Black squares represent the mean; bars, SEMs.
- See also Figure S1.

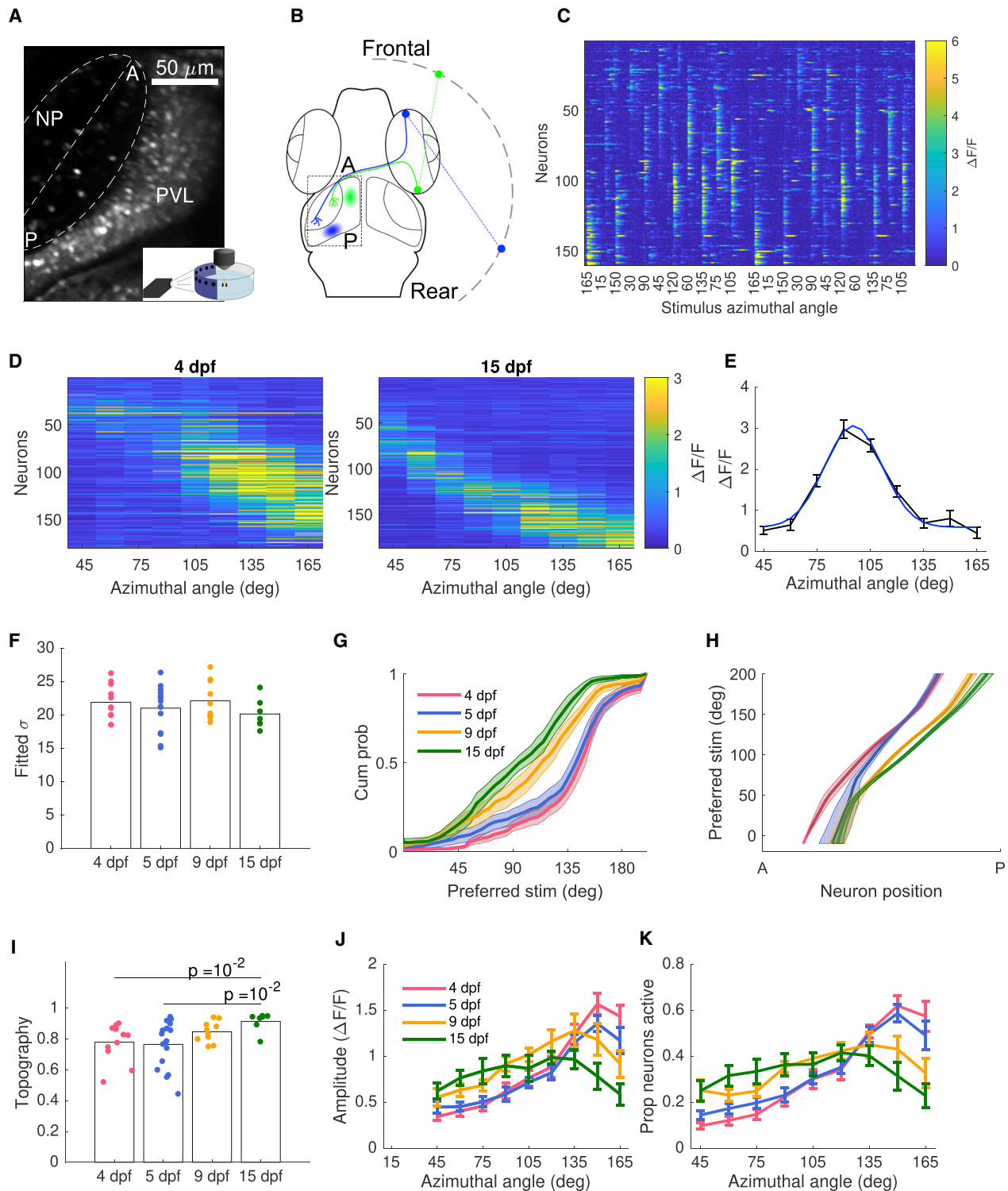


Figure 2. Changes in Neural Representation across the Visual Field at 70- μ m Depth

(A) An example tectal image from a 15-dpf fish. The neuropil (NP) contour of each fish was fitted with an ellipse, with the major axis defining the tectal anterior-posterior (AP) axis. Periventricular layer (PVL), NP, anterior (A), and posterior (P) ends of the tectum are indicated. Inset: larvae were embedded in agarose with one eye facing the projected image for 2-photon calcium imaging. We recorded evoked activity at a depth of 70 μ m in response to 20 trials of the stimulus set consisting of spots at positions 45°, 60°, 75°, 90°, 105°, 120°, 135°, 150°, and 165° of the visual field, where 0° was defined as the body axis.

(legend continued on next page)

180 spot presentations per fish (Figure 2A). Although movement has been shown to also be a relevant cue [23], our primary concern here was the fish's ability to spatially localize stimuli. At this depth, spots at azimuthal angles less than 45° relative to the fish's midline failed to elicit robust responses (an issue we return to shortly), consistent with some published literature (see Discussion). We therefore focused on spots at angles from 45° to 165°. Consistent with broad tectal receptive fields previously reported [7, 20, 27], each spot in the visual field elicited a response in a population of many cells. These population responses roughly matched the topographic retinotectal organization whereby spots in the frontal visual field (i.e., angles up to 90 degrees) elicited neural responses in the anterior tectum (Figures 2B and 2C).

The receptive field of each neuron was calculated by averaging its response amplitude over stimuli repetitions (Figure 2D). We fitted each neuron's raw receptive field with a Gaussian function with baseline offset (see STAR Methods) (Figure 2E), and the angle at which the Gaussian peaked was defined as the neuron's preferred stimulus. There was no change in receptive field width over development (Figure 2F). While at all ages, we collected responses representing a large extent of the visual field (Figure S2A), at 4 dpf, the proportion of neurons tuned for the positions stimulated in the frontal visual field (45° to 75°) was much lower than for the rear visual field; however, this tuning bias balanced over development with roughly even representation of the visual field by 15 dpf (Figure 2G). We then examined the relation between the position of the neurons on the anterior-posterior (AP) axis of the tectum and their tuning and observed a shift of the tectal map with age (Figure 2H). This was not due to a change in eye position over development (Figure S2B). We further quantified topography as the correlation coefficient per fish between the preferred stimuli of neurons and their position on the AP axis. Topography was more precise at 15 dpf compared to 4 dpf and showed decreased variability for 9 and 15 dpf combined compared to 4 and 5 dpf combined (Figure 2I).

In addition to functional changes at the single-neuron level, there were also substantial changes in the statistics of the neural response at the population level. At 4 dpf, response strength in the rear visual field was much higher compared to the positions

stimulated in the frontal visual field. However, over development, the strength of rear responses decreased while the strength of these frontal responses increased (Figure 2J). There was a similar pattern for the proportion of neurons active (Figure 2K). Thus, at this depth in the tectum, the representation of the visual field exhibits substantial spatial and functional changes over development, with a large increase in response strength to the positions stimulated in the frontal visual field (45° to 75°).

The above data addressed responses at 70 μm depth to spots starting at 45°, since smaller angles did not produce strong responses. To test whether stronger frontal responses could be obtained from other tectal depths, for a new set of fish, we presented spots at 15°, 30°, 45°, and 60° at depths of 55, 70, 85, and 100 μm at ages 5 and 9 dpf. At 5 dpf, tectal responses to these spots were strongest at 100 μm (Figure 3A); however, by 9 dpf, response strength did not vary with depth (Figure 3B). We then more systematically investigated how responses at 100 μm varied across the entire visual field from 15° to 165° and over development (ages 5 and 13–15 dpf). We observed no change in the width of receptive fields over development (Figure 3C), similar to the results observed at 70 μm. However, unlike the response at 70 μm, there was a roughly even representation of the visual field at both 5 and 15 dpf (Figure 3D). The tectal spatial map was relatively constant over development (Figure 3E) and displayed a similar degree of topography over development (Figure 3F). At the population level, the response strength and proportion of active neurons was age dependent but stable across the visual field (Figures 3G and 3H). The contrast between relative stability at a depth of 100 μm and clear developmental trends at 70 μm suggests that circuit development in the tectum is a spatially heterogeneous process, but nonetheless involves systematic shifts in visual representation.

Decoding Performance Improves Nonuniformly over Development

The results so far demonstrate that tectal circuits undergo substantial functional changes at the single-neuron and the population level between 4 and 15 dpf. We next asked whether these circuitry changes are reflected in the performance of decoding spatial information and, furthermore, whether they are correlated with hunting performance. We first focused on the recordings

(B) Schematic of retinotectal projection showing temporal retinal ganglion cells (green, representing the frontal visual field) projecting to anterior tectum and nasal ganglion cells (blue, representing the rear visual field) projecting to posterior tectum. The dashed black rectangle represents the tectal region shown in (A).

(C) Population response of 187 PVL neurons from the fish shown in (A) elicited by two trials of visual stimuli set. Neurons are sorted by their position on the AP axis.

(D) Raw receptive fields of 217 and 187 PVL neurons in an example 4 dpf (left) and 15 dpf (right) fish, respectively. Neurons are sorted by their position on the AP axis and display a rough topography.

(E) Raw (black) and fitted (blue) receptive field of an example neuron from a 15 dpf fish shown in (C) and (D) (neuron 123).

(F) Mean receptive field width did not change over development (t test).

(G) More neurons were tuned to the rear visual field at 4 dpf, but this gradually balanced over development. Shading represents SEMs. Comparing the area under the curve grouped by age showed differences as follows: 4 versus 5, n.s.; 4 versus 9, $p = 0.01$; 4 versus 15, $p = 10^{-3}$; one-way ANOVA with Bonferroni multiple-comparison correction.

(H) Neuronal selectivity shifted over development so that at each tectal position, neuronal tuning moved in a frontal direction. Shading represents SEMs. A linear fit to these curves showed similar slopes but different intersection points with the x axis, indicating that maps are shifted (4 versus 15, $p = 0.18$, for slopes, and $p = 0.04$ for intercepts t test).

(I) Topography improved over development (two-sample t test). Variability also decreased over development (4 and 5 versus 9 and 15, $p = 10^{-2}$, two-sample F-test).

(J) At 4 dpf, the population response amplitude was stronger in response to the rear visual field, but this balanced over development to give a more even response amplitude to stimuli across the visual field.

(K) At 4 dpf, a larger proportion of neurons were active in response to stimuli in the rear visual field, but again, this balanced over development.

See also Figure S2.

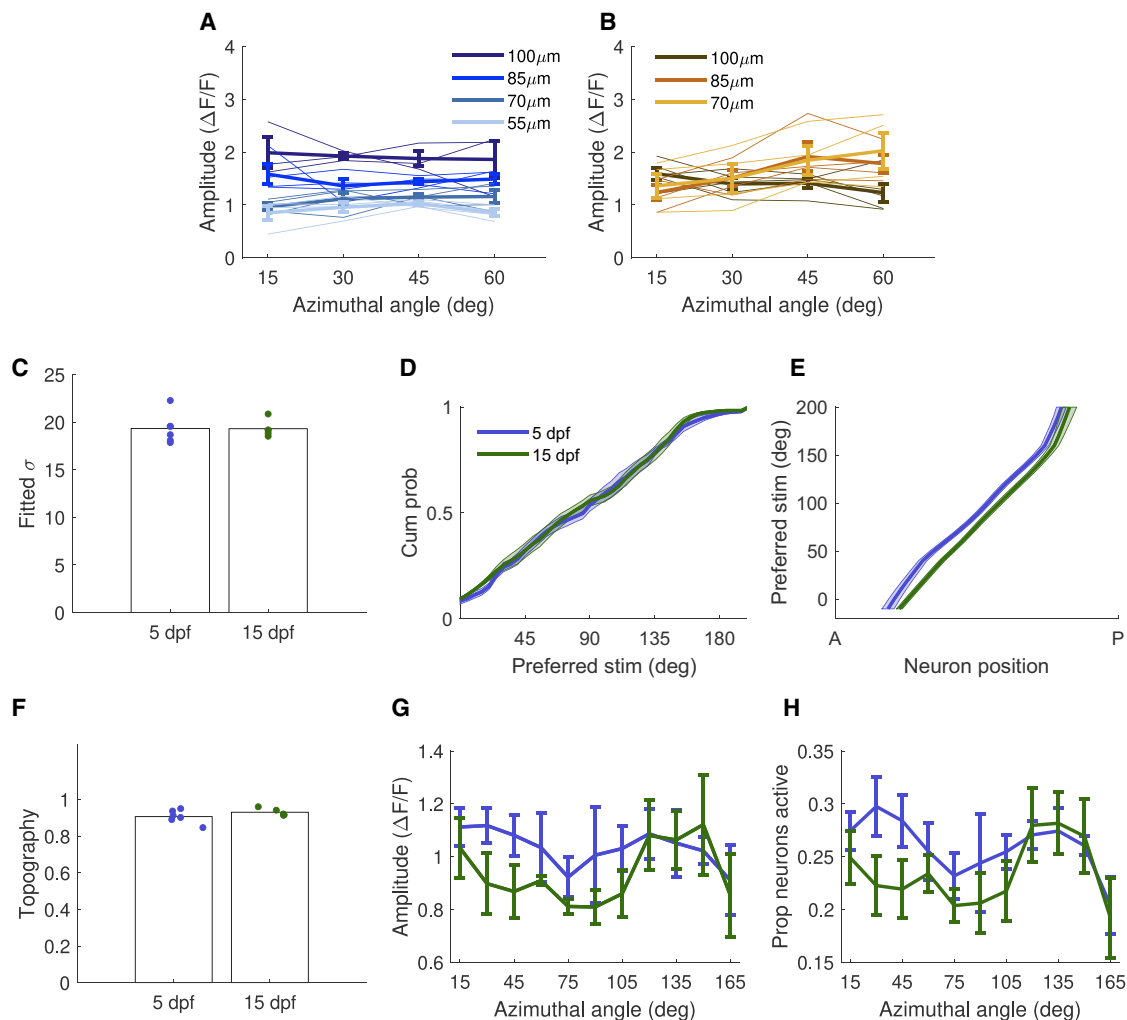


Figure 3. Neural Representations Are Steady across the Visual Field at 100- μm Depth

- (A) Mean responses at different tectal depths over four repetitions of four anterior stimuli. At 5 dpf, response amplitude was higher for 100- μm depth compared to responses at 55, 70, and 85 μm ($p = 10^{-11}$). No effect of stimulus or interaction stimulus:depth was found ($p = 0.98$ and $p = 0.87$, respectively, two-way ANOVA, Tukey-Kramer multiple comparison correction, $n = 4$ [55 μm], $n = 4$ [70 μm], $n = 4$ [85 μm], $n = 3$ [100 μm]).
- (B) At 9 dpf, there was no difference in response strength across tectal depths ($p = 0.13$). No effect of stimulus or interaction stimulus:depth was found ($p = 0.14$ and $p = 0.14$, respectively, two-way ANOVA, Tukey-Kramer multiple comparison correction, $n = 4$ [70 μm], $n = 4$ [85 μm], $n = 5$ [100 μm]).
- (C) Mean receptive field width at 100- μm depth did not change over development (5 and 13–15 dpf, $n = 6, 5$ respectively, different fish for each age, older group is referred to as 15 dpf).
- (D) Tuning proportion across the visual field was similar over development. Comparing the area under the curves grouped by age showed no difference over development ($p = 0.63$; one-way ANOVA).
- (E) Neuronal selectivity was unchanged over development. Shading represents SEMs. A linear fit for each fish showed no difference in the slopes or in intersection points with the x axis over development ($p = 0.57$, $p = 0.17$ respectively, two-sample t test).
- (F) Topography values were stable over development ($p = 0.23$ two-sample t test), and there was no difference in the variability of this measure over development ($p = 0.17$, two-sample F-test).
- (G) Population response amplitude across the visual field over development. Amplitude was age dependent ($p = 0.04$); however, stimulus identity or the interaction between stimulus and age had no impact on population response strength ($p = 0.41$, $p = 0.92$ respectively, multiple regression analysis).
- (H) Proportion of neurons active in response to stimuli was not different across the visual field. This proportion was age dependent ($p = 0.03$); however, stimulus identity or the interaction between stimulus and age had no impact ($p = 0.07$, $p = 0.84$, respectively, multiple regression analysis).

from 70- μm depth. Using a linear decoder, we quantified the relation between the original stimulus and the decoded stimuli position (Figures 4A–4D) (results were qualitatively similar for other decoders [Figure S3A]). Decoding performance in older fish was higher when averaged across the entire visual field compared to younger animals (Figure 4E). This improvement

was due to improvement toward the frontal visual field: mean decoding performance for 45° to 75° stimuli averaged over fish increased over development (Figure 4F). By 15 dpf, performance was high and uniform over the entire visual field (Figure 4G). Notably, the improvement in decoding occurred despite there being no sharpening of receptive fields (Figure 2F). At 100- μm

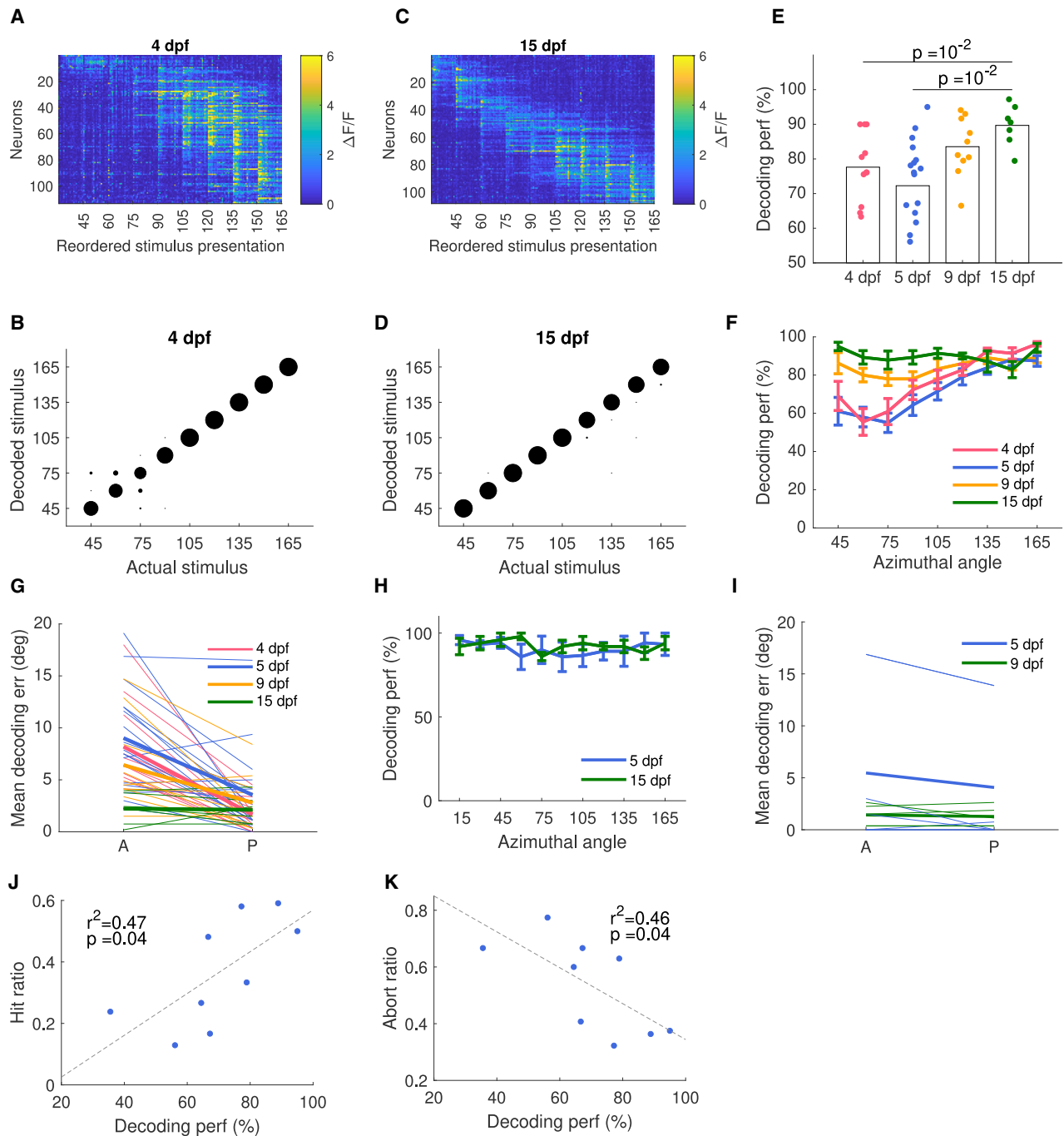


Figure 4. Decoding of Stimuli Improves Non-uniformly over Development at 70- μ m Depth

(A) Population responses grouped and reordered by the stimulus presented in an example 4-dpf fish at 70- μ m depth.
 (B) Decoded stimuli for each of the 20 presentations of each stimulus as shown in (A). Dot size is proportional to the fraction of presentations that decoded to a particular stimulus value.
 (C and D) Same as (A) and (B) for an example 15-dpf fish, showing better performance than the 4-dpf fish.
 (E) Decoding performance over all stimuli per fish improved over development at 70- μ m depth (two-sample t test).
 (F) Decoding performance became more even across the visual field with age. Error bars, SEMs.
 (G) Decoding error for the most frontal two spots and the rear-most two spots for each fish (thin lines) and the averaged error per age (thick colored lines) at different ages showed better decoding performance of rear visual stimuli at 4, 5, and 9 dpf (4 dpf, $p = 10^{-3}$; 5 dpf, $p = 10^{-3}$; 9 dpf, $p = 10^{-2}$; paired-sample t test) but no difference at 15 dpf.
 (H) At 100- μ m depth, decoding performance was stable across the visual field and with age.

(legend continued on next page)

depth, decoding did not vary with position and age (Figures 4H and 4I).

At 70- μm depth, there was notable individual variation in decoding performance within an age group, particularly at 5 dpf, when zebrafish are normally just beginning to hunt prey. We therefore asked whether these differences were related to the ability of larvae to catch prey. There was indeed a correlation between decoding performance and hunting hit ratio per fish for the nine 5-dpf fish for which we had both behavioral and imaging data (Figure 4J). There was no dependence of hit ratio on fish length for the 5-dpf fish (Figure S3B), indicating that the correlation between hit ratio and decoding was not simply due to different levels of maturity within the 5-dpf population. There was a significant (negative) correlation between decoding performance and abort ratio (Figure 4K) and a positive though non-significant trend between decoding and hit ratio when abort events were excluded (Figure S3C). Thus, tectal decoding performance at 70- μm depth can directly predict the prey-capture abilities of individual fish, suggesting that individual differences in the ability to spatially localize prey at this depth in the tectum could constrain hunting performance.

Information Encoded in Neural Responses Shifts and Increases over Development

To further investigate the spatiotemporal changes in tectal coding at 70- μm depth, we next investigated how response entropy and mutual information were distributed across the tectum, and how these distributions changed with development. For this analysis, we divided the stimuli into three subsets: 45°, 60°, and 75° (“frontal”); 90°, 105°, and 120° (“middle”), and 135°, 150°, and 165° (“rear”). We computed each neuron’s response entropy for each stimulus subset. Entropy showed localized increases on the AP axis consistent with the presence of a topographic organization (Figures 5A–5C, left). We fitted the averaged entropy curves with a Gaussian function with baseline offset and examined peak entropy position. Consistent with an increasing proportion of neurons responsive to stimuli at 45°, 60°, and 75° (Figure 2K), there was an increase in the entropy for these stimuli over development (Figure 5A) and a shift toward a more posterior peak of entropy for all stimulus subsets in the tectum (Figures 5A–5C, right), consistent with Figure 2H.

For each neuron, we then computed the mutual information between the neuron’s response and the different stimulus subsets (example shown in Figure 5G) and examined the average mutual information along the AP axis (Figures 5D–5F, left). The center of mass of these distributions shifted posteriorly in the tectum for all stimulus subsets (Figures 5D–5F, right), indicating a shift in stimulus information. However, this mutual information distribution along the AP axis was quite variable and, in some cases, appeared bimodal (Figures 5D–5F, left, example shown in Figure 5G, see also Figure S4A). To examine the source of this variability, we considered a model of Bernoulli neurons with Gaussian receptive fields and tuning that tiled the visual field

(Figure S4B, see STAR Methods). The model allowed us to relate the mutual information between the activity of single neurons and the stimuli to the variance of the neurons’ response probability to the different stimuli and suggested that high mutual information values are achieved for neurons with high variability (Figures S4C and S4D). We then used the model to examine the distribution of mutual information for a population of neurons and showed that as receptive field size was increased, the local unimodal distributions of mutual information around each stimulus position merged to a global bimodal distribution (Figures S4E and S4F). This bimodal distribution was observed even when the map was irregular (Figure S4G, see STAR Methods), consistent with experimental results (Figure S4A, middle). Thus, the bimodality seen in our data (Figure S4A) can be straightforwardly explained by a simple computational model.

Finally, we considered the mean mutual information between the different stimulus subsets over all neurons (Figure 5H). At 4 and 5 dpf, information about rear stimuli was higher than stimuli at 45°, 60°, and 75°, consistent with higher decoding performance of rear stimuli at these ages. Over development, there was an increase in mean mutual information for the stimuli at 45°, 60°, and 75°, consistent with improved decoding performance of these stimuli. Together, these results show that stimulus-related information increased over development overall, but that this increase was restricted to certain portions of the visual field.

DISCUSSION

By analyzing behavior over a period in which zebrafish are learning to hunt fast-moving prey, we found that their hunting performance improves, indicating that this is a highly dynamic period in their development (Figure 1). We then showed that these improvements can be linked to improvements in sensory coding in certain parts of the tectum (Figure 4). In particular, we showed that early in development, the rear visual stimuli elicit stronger and denser responses in a particular plane of the tectum compared to more frontal stimuli and that this bias balances over development. While increasing levels of fine-motor control also likely contribute to the increase in hunting effectiveness (for instance, changes in fin and body morphology can influence the generation of locomotor forces [28] and fish hydrodynamics [29]), we demonstrated a clear correlation between hunting efficiency and coding efficiency at one depth in the tectum.

An interesting developmental progression in our behavioral data is that fish become increasingly better aligned with the prey after the first bout of the hunting event (Figure 1I). While this is consistent with a gradual improvement in prey localization in the frontal visual field over development, an alternative explanation is that it is due to improvements in the motor system. However, in both cases, it remains to be explained why the turn is usually an undershoot, rather than errors being randomly

(I) At 100- μm depth, there was no difference in decoding error of frontal and rear spots in both 5 and 15 dpf (5 dpf $p = 0.49$; 15 dpf $p = 0.68$; paired-sample t test).

(J) Hit ratio for individual 5-dpf fish was correlated with their decoding performance from 70- μm depth.

(K) Abort ratio for individual 5-dpf fish was correlated with their decoding performance.

See also Figure S3.

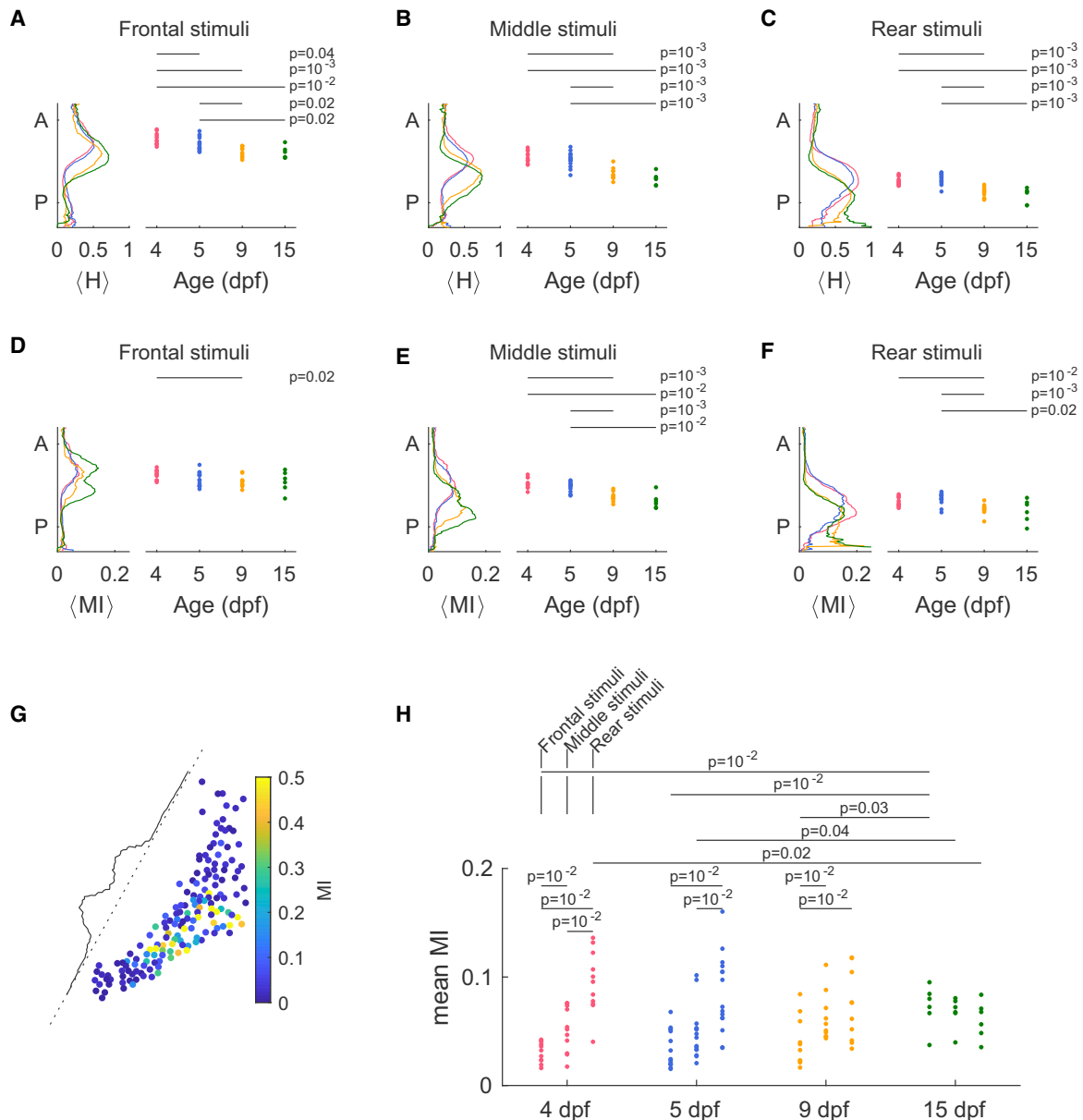


Figure 5. Information about Visual Field Position Increases Non-uniformly over Development.

(A) Average entropy distribution along the AP axis for the frontal stimuli (left) and the respective peak position of the fitted curves (right) indicating a spatial shift in information over development. (B) Same as (A) for the middle stimuli. (C) Same as (A) for the rear stimuli. (D) Mean mutual information distribution along the AP axis for the frontal stimuli (left) and the distribution's center of mass (right) show a posterior shift in mutual information over development. (E) Same as (D) for the middle stimuli. (F) Same as (D) for the rear stimuli.

(G) Example of the distribution of mutual information for the three middle stimuli across the optic tectum of a 9 dpf fish, and the respective mean MI along the AP axis.

(H) Mean mutual information for the three stimulus sets over development. Mean mutual information increases over development for the three most frontal stimuli. All tests Wilcoxon rank-sum.

See also Figure S5.

distributed between overshoots and undershoots. This undershoot, previously observed in 5–7-dpf larval zebrafish, is not a predictive effect [30]. Recently, undershoots were identified not only in the first bout but also in subsequent pursuit bouts during the event in 7–8-dpf larval zebrafish, suggesting a stochastic recursive strategy for localization of prey [14]. It was proposed

that this stochastic recursive model allows less locomotive kinetic energy spent during the event compared to an ideal-choice model [14]. However, this model does not explain why the undershoot would decrease over development. One possibility is that, assuming the energy required for the turn increases with the turn angle, a second corrective turn after an undershoot requires less

summed energy for both turns than a second corrective turn after an overshoot. In this case, the optimal degree of undershoot for an energy efficient strategy would depend on the uncertainty of estimates of prey location and velocity. Therefore, increased visual acuity based on improved sensory coding over development may reduce the extent to which undershoot is necessary to maintain an optimal strategy for energy efficient hunting.

One question raised by our work regards the role of eye convergence for hunting. A clear rationale for this at the final stage of prey capture, when the fish strikes from close range toward a target positioned directly in front of the fish, is that it provides depth information via binocular vision [23]. Indeed, unilateral lensectomy of 7-dpf larval zebrafish showed that the spatial distribution of prey position immediately prior to capture strikes was less localized in unilaterally delensed fish than in controls [16]. Furthermore, fish without binocular vision are less likely to perform a capture strike, emphasizing the importance of binocular cues for positioning prey in a preferred strike zone [16]. However, it has also been shown that binocular vision is not required for the initiation of hunting events [16]. Hence, it remains unclear why eye convergence first occurs at the initial stage of a hunting event, when the prey is distant and misaligned with the fish for binocular cues to be relevant. A possible rationale for initial convergence raised by our work is that it moves the image of the prey toward the nasal retina and thus toward the posterior tectum, where spatial decoding of position is initially superior (Figure 4F).

The temporal region of the retina, which is stimulated by objects in the frontal visual field and innervates the anterior part of the tectum (Figure 2B), is the last retinal region to differentiate at 5–7 dpf [30]. This retinal temporal region exhibits a high density of cones, likely providing high-acuity vision in the corresponding region of the visual field [31, 32]. Thus, part of the improvement we observed in both hunting performance and tectal decoding of frontal stimuli could have a retinal origin. While the retina grows in concentric annuli [33], the optic tectum grows by adding new neurons at its posterior end [34, 35]. These neurons then migrate anteriorly in the tectum and become tuned to more frontal stimuli [34], consistent with our results. Projections from the tectum to premotor areas have some topographic organization [36], suggesting that a simple topography-based code could provide the substrate for visuo-motor transformations. However, due to the highly dynamic nature of the tectal map (for instance, at 70- μ m depth, we found shifts in tuning of around 50° at each tectal position between 4 and 15 dpf [Figure 2H]), such a topography-based code would presumably require matched plasticity in downstream structures. Topography-based codes for spatial position also have lower performance than more statistically motivated codes [21]. Together, these findings suggest that coding strategies for spatial localization may be more sophisticated than topographic mapping alone.

We observed differences in the trajectory of tectal coding development between 70 μ m and 100 μ m imaging depths. The tectum is a complex 3D structure [37], and it is unlikely that either of these depths corresponds to biologically meaningful functional subdivisions of the tectum. Rather, they each give a spatial snapshot of how complex 3D circuits are emerging over development. In future work, technologies like galvo-scanning 2-photon or light sheet microscopy could be employed to give a

more complete picture by imaging multiple tectal planes simultaneously.

The finding that decoding quality was already high for frontal stimuli at 5 dpf at 100- μ m depth raises the question of why changes in decoding quality with age at 70- μ m depth might nevertheless affect behavior. It is currently unknown how information from different parts of the tectum representing the same position in visual space is combined by downstream structures. One possibility is a “winner take all” model, where for each visual field position, a downstream area listens only to the tectal neurons that are most informative for that stimulus, in a way that changes over development. An alternative “integrative” model is that for each stimulus, a downstream structure integrates information from all neurons representing that stimulus, irrespective of relative levels of information content about that stimulus. While our present results are consistent with this latter model, further work will be required to determine if there is indeed a causal rather than just correlational link between improvements in coding at 70- μ m depth over development and improvements in hunting behavior.

Our finding of an initial over-representation of the rear visual field is consistent with previous work using the independent measure of tectal spontaneous activity. Inspecting the activation frequency and density of spontaneous tectal neural assemblies [20], posterior tectal assemblies showed higher activation levels and higher density compared to more anterior assemblies. The developmental trajectory of these assemblies showed denser posterior assemblies compared to anterior assemblies at 3 dpf, and this bias mostly disappeared by 8 dpf [19]. Denser responses to stimuli in the rear visual field were also evident when neural responses were tracked during a hunting event in freely swimming 6–8-dpf fish [38] (their Extended Data Figure 5). In this example, the highest number of tectal neurons active in response to prey detection occurred in the rear visual field (105 degrees), and the lowest number in the frontal visual field (15 degrees). Thus, our findings are consistent with several previous reports suggesting a developmental progression in the representation of the visual world.

We showed that individual differences in behavioral performance could be predicted by the quality of decoding from neural activity in the tectum (Figure 4J). In humans, relating fMRI measurements to individual differences in psychological traits is a rapidly expanding area [39]. For instance, [40] showed that variations in the size of primary visual cortex could predict individual differences in visual perception, and it has been demonstrated that individual functional connectivity profiles can predict fluid intelligence [41] and creativity [42]. However, as far as we are aware, ours is among the first demonstrations that neural decoding can be used to predict behavior at an individual level (cf. [43]). A caveat of our work is that the correlation between decoding and behavior is based on our main dataset from 70- μ m depth, where we did not record responses to stimuli at angles less than 45°. Since in contrast, the majority of hunting events were initiated for prey angles more frontal than this (Figure 1G), it remains to be determined how tectal responses for correspondingly small angles might be correlated with hunting performance.

The changes we observed in hunting performance that correlated with neural decoding could largely be attributed to changes in the abort rate. This connection between neural decoding and the likelihood of an abort might be explained by a sensory

feedback loop required to maintain the hunting state. The possibility of such a feedback loop was proposed by [16], who demonstrated that larval zebrafish require continuous visual feedback to sustain prey capture behavior through to a strike. Trivedi and Bollmann [24] found that intervals between bouts were longer when post-bout visual feedback was delayed or positioned unexpectedly in a restrained virtual-reality prey-capture assay. Further, they showed that virtual prey must increase in size and velocity during a hunt sequence, simulating approach toward the prey, to elicit monotonically decreasing inter-bout intervals as typically observed during hunting events. Mearns et al. [16] found that fish will abort hunting immediately when virtual prey are made to vanish in a free-swimming virtual-reality prey-capture assay. Statistical analysis of prey capture in free swimming has shown that larval zebrafish may also be integrating predictions of prey trajectories in the visuomotor transformation [14, 15]. We therefore suggest that a sufficiently large mismatch between prediction and post-bout sensory feedback may trigger an abort. Increased efficacy of neural coding presumably decreases the likelihood of large prediction error that might arise due to either incorrect prediction or incorrect post-bout sensory feedback. Together, this provides an explanation for our finding that neural decoding performance is negatively correlated with abort rate.

Due to its unique advantages, the larval zebrafish has proven to be a very effective model for addressing fundamental questions about brain function at the systems level. However, we have shown that both behavior and neural coding in the optic tectum show significant refinement between 4 and 15 dpf. The larval fish brain at this stage is likely undergoing highly dynamic processes of development across many different systems simultaneously. It will be instructive in future work to determine the degree to which neural mechanisms found in larvae generalize to adults.

STAR★METHODS

Detailed methods are provided in the online version of this paper and include the following:

- **KEY RESOURCES TABLE**
- **RESOURCE AVAILABILITY**
 - Lead Contact
 - Materials Availability
 - Data and Code Availability
- **EXPERIMENTAL MODEL AND SUBJECT DETAILS**
 - Zebrafish
- **METHOD DETAILS**
 - Hunting behavior assay
 - Imaging hunting behavior of individuals over development
 - Analysis of hunting behavior movies
 - 2-photon calcium imaging
 - Visual stimulation
 - Automatic cell detection
 - Tuning curves
 - Decoding stimulus identity
 - Information theory analysis
 - Modeling information theory results
- **QUANTIFICATION AND STATISTICAL ANALYSIS**

SUPPLEMENTAL INFORMATION

Supplemental Information can be found online at <https://doi.org/10.1016/j.cub.2020.06.040>.

ACKNOWLEDGMENTS

We gratefully acknowledge funding from Australian Research Council grants DP170102263 and DP180100636. Imaging was performed at the Queensland Brain Institute's Advanced Microscopy Facility using a Zeiss LSM 710 2-photon microscope, generously supported by the Australian Government through the ARC LIEF grant LE130100078.

AUTHOR CONTRIBUTIONS

Conceptualization, L.A. and G.J.G.; Methodology, L.A., Z.P., S.Z., and G.J.G.; Software, L.A., J.M., and M.M.; Formal Analysis, L.A., J.M., and M.M.; Investigation, L.A., Z.P., J.M., M.M., S.Z., B.S., and A.M.; Writing – Original Draft, L.A., J.M., and G.J.G.; Writing – Review & Editing, L.A., Z.P., J.M., M.M., S.Z., B.S., A.M., and G.J.G.; Supervision, G.J.G.; Funding Acquisition, G.J.G.

DECLARATION OF INTERESTS

The authors declare no competing interests.

Received: November 25, 2019

Revised: April 13, 2020

Accepted: June 11, 2020

Published: July 23, 2020; corrected online: August 7, 2020

REFERENCES

1. Avitan, L., and Goodhill, G.J. (2018). Code under construction: neural coding over development. *Trends Neurosci.* *41*, 599–609.
2. Levelt, C.N., and Hübener, M. (2012). Critical-period plasticity in the visual cortex. *Annu. Rev. Neurosci.* *35*, 309–330.
3. Ko, H., Cossell, L., Baragli, C., Antolik, J., Clopath, C., Hofer, S.B., and Mrsic-Flogel, T.D. (2013). The emergence of functional microcircuits in visual cortex. *Nature* *496*, 96–100.
4. Smith, G.B., Sederberg, A., Elyada, Y.M., Van Hooser, S.D., Kaschube, M., and Fitzpatrick, D. (2015). The development of cortical circuits for motion discrimination. *Nat. Neurosci.* *18*, 252–261.
5. Chevée, M., and Brown, S.P. (2018). The development of local circuits in the neocortex: recent lessons from the mouse visual cortex. *Curr. Opin. Neurobiol.* *53*, 103–109.
6. Brust, V., Schindler, P.M., and Lewejohann, L. (2015). Lifetime development of behavioural phenotype in the house mouse (*Mus musculus*). *Front. Zool.* *12* (Suppl 1), S17.
7. Niell, C.M., and Smith, S.J. (2005). Functional imaging reveals rapid development of visual response properties in the zebrafish tectum. *Neuron* *45*, 941–951.
8. Kita, E.M., Scott, E.K., and Goodhill, G.J. (2015). The influence of activity on axon pathfinding in the optic tectum. *Dev. Neurobiol.* *75*, 608–620.
9. Borla, M.A., Palecek, B., Budick, S., and O'Malley, D.M. (2002). Prey capture by larval zebrafish: evidence for fine axial motor control. *Brain Behav. Evol.* *60*, 207–229.
10. Portugues, R., and Engert, F. (2009). The neural basis of visual behaviors in the larval zebrafish. *Curr. Opin. Neurobiol.* *19*, 644–647.
11. Muto, A., Ohkura, M., Abe, G., Nakai, J., and Kawakami, K. (2013). Real-time visualization of neuronal activity during perception. *Curr. Biol.* *23*, 307–311.
12. McElligott, M.B., and O'Malley, D.M. (2005). Prey tracking by larval zebrafish: axial kinematics and visual control. *Brain Behav. Evol.* *66*, 177–196.

13. Marques, J.C., Lackner, S., Félix, R., and Orger, M.B. (2018). Structure of the Zebrafish Locomotor Repertoire Revealed with Unsupervised Behavioral Clustering. *Curr. Biol.* **28**, 181–195.
14. Bolton, A.D., Haesemeyer, M., Jordi, J., Schaehtle, U., Saad, F.A., Mansinghka, V.K., Tenenbaum, J.B., and Engert, F. (2019). Elements of a stochastic 3D prediction engine in larval zebrafish prey capture. *eLife* **8**, e51975.
15. Johnson, R.E., Linderman, S., Panier, T., Wee, C.L., Song, E., Herrera, K.J., et al. (2020). Probabilistic Models of Larval Zebrafish Behavior Reveal Structure on Many Scales. *Curr. Biol.* **30**, 70–82.
16. Mearns, D.S., Donovan, J.C., Fernandes, A.M., Semmelhack, J.L., and Baier, H. (2020). Deconstructing Hunting Behavior Reveals a Tightly Coupled Stimulus-Response Loop. *Curr. Biol.* **30**, 54–69.
17. Westphal, R.E., and O'Malley, D.M. (2013). Fusion of locomotor maneuvers, and improving sensory capabilities, give rise to the flexible homing strikes of juvenile zebrafish. *Front. Neural Circuits* **7**, 108.
18. Avitan, L., Pujic, Z., Mölter, J., Van De Poll, M., Sun, B., Teng, H., et al. (2017). Spontaneous activity in the zebrafish tectum reorganizes over development and is influenced by visual experience. *Curr. Biol.* **27**, 2407–2419.
19. Pietri, T., Romano, S.A., Pérez-Schuster, V., Boulanger-Weill, J., Candat, V., and Sumbre, G. (2017). The emergence of the spatial structure of tectal spontaneous activity is independent of visual inputs. *Cell Rep.* **19**, 939–948.
20. Romano, S.A., Pietri, T., Pérez-Schuster, V., Jouary, A., Haudrechy, M., and Sumbre, G. (2015). Spontaneous neuronal network dynamics reveal circuit's functional adaptations for behavior. *Neuron* **85**, 1070–1085.
21. Avitan, L., Pujic, Z., Hughes, N.J., Scott, E.K., and Goodhill, G.J. (2016). Limitations of neural map topography for decoding spatial information. *J. Neurosci.* **36**, 5385–5396.
22. Kimmel, C.B., Ballard, W.W., Kimmel, S.R., Ullmann, B., and Schilling, T.F. (1995). Stages of embryonic development of the zebrafish. *Dev. Dyn.* **203**, 253–310.
23. Bianco, I.H., Kampff, A.R., and Engert, F. (2011). Prey capture behavior evoked by simple visual stimuli in larval zebrafish. *Front. Syst. Neurosci.* **5**, 101.
24. Trivedi, C.A., and Bollmann, J.H. (2013). Visually driven chaining of elementary swim patterns into a goal-directed motor sequence: a virtual reality study of zebrafish prey capture. *Front. Neural Circuits* **7**, 86.
25. Bianco, I.H., and Engert, F. (2015). Visuomotor transformations underlying hunting behavior in zebrafish. *Curr. Biol.* **25**, 831–846.
26. Gahtan, E., Tanger, P., and Baier, H. (2005). Visual prey capture in larval zebrafish is controlled by identified reticulospinal neurons downstream of the tectum. *J. Neurosci.* **25**, 9294–9303.
27. Sajovic, P., and Levinthal, C. (1982). Visual cells of zebrafish optic tectum: mapping with small spots. *Neuroscience* **7**, 2407–2426.
28. McHenry, M.J., and Lauder, G.V. (2006). Ontogeny of form and function: locomotor morphology and drag in zebrafish (*Danio rerio*). *J. Morphol.* **267**, 1099–1109.
29. Müller, U.K., and van Leeuwen, J.L. (2004). Swimming of larval zebrafish: ontogeny of body waves and implications for locomotory development. *J. Exp. Biol.* **207**, 853–868.
30. Patterson, B.W., Abraham, A.O., MacIver, M.A., and McLean, D.L. (2013). Visually guided gradation of prey capture movements in larval zebrafish. *J. Exp. Biol.* **216**, 3071–3083.
31. Schmitt, E.A., and Dowling, J.E. (1999). Early retinal development in the zebrafish, *Danio rerio*: light and electron microscopic analyses. *J. Comp. Neurol.* **404**, 515–536.
32. Zimmermann, M.J.Y., Nevala, N.E., Yoshimatsu, T., Osorio, D., Nilsson, D.E., Berens, P., et al. (2018). Zebrafish Differentially Process Color across Visual Space to Match Natural Scenes. *Curr. Biol.* **28**, 2018–2032.
33. Reh, T.A., and Constantine-Paton, M. (1983). Qualitative and quantitative measures of plasticity during the normal development of the *Rana pipiens* retinotectal projection. *Brain Res.* **312**, 187–200.
34. Boulanger-Weill, J., Candat, V., Jouary, A., Romano, S.A., Pérez-Schuster, V., and Sumbre, G. (2017). Functional interactions between newborn and mature neurons leading to integration into established neuronal circuits. *Curr. Biol.* **27**, 1707–1720.
35. Boulanger-Weill, J., and Sumbre, G. (2019). Functional integration of newborn neurons in the zebrafish optic tectum. *Front. Cell Dev. Biol.* **7**, 57.
36. Helmbrecht, T.O., Dal Maschio, M., Donovan, J.C., Koutsouli, S., and Baier, H. (2018). Topography of a visuomotor transformation. *Neuron* **100**, 1429–1445.
37. Scott, E.K., and Baier, H. (2009). The cellular architecture of the larval zebrafish tectum, as revealed by gal4 enhancer trap lines. *Front. Neural Circuits* **3**, 13.
38. Marques, J.C., Li, M., Schaak, D., Robson, D.N., and Li, J.M. (2020). Internal state dynamics shape brainwide activity and foraging behaviour. *Nature* **577**, 239–243.
39. Dubois, J., and Adolphs, R. (2016). Building a Science of Individual Differences from fMRI. *Trends Cogn. Sci.* **20**, 425–443.
40. Schwarzkopf, D.S., Song, C., and Rees, G. (2011). The surface area of human V1 predicts the subjective experience of object size. *Nat. Neurosci.* **14**, 28–30.
41. Finn, E.S., Shen, X., Scheinost, D., Rosenberg, M.D., Huang, J., Chun, M.M., Papademetris, X., and Constable, R.T. (2015). Functional connectome fingerprinting: identifying individuals using patterns of brain connectivity. *Nat. Neurosci.* **18**, 1664–1671.
42. Beaty, R.E., Seli, P., and Schacter, D.L. (2019). Network neuroscience of creative cognition: mapping cognitive mechanisms and individual differences in the creative brain. *Curr. Opin. Behav. Sci.* **27**, 22–30.
43. Honegger, K.S., Smith, M.A.Y., Churgin, M.A., Turner, G.C., and de Bivort, B.L. (2019). Idiosyncratic neural coding and neuromodulation of olfactory individuality in *Drosophila*. *Proceedings of the National Academy of Sciences*. <https://doi.org/10.1073/pnas.1901623116>.
44. Vladimirov, N., Mu, Y., Kawashima, T., Bennett, D.V., Yang, C.T., Looger, L.L., Keller, P.J., Freeman, J., and Ahrens, M.B. (2014). Light-sheet functional imaging in fictively behaving zebrafish. *Nat. Methods* **11**, 883–884.
45. Westerfield, M. (1995). *The zebrafish book: a guide for the laboratory use of zebrafish (Brachydanio rerio)* (Eugene: University of Oregon Press).
46. Bolme, D.S., Beveridge, J.R., Draper, B.A., and Lui, Y.M. (2010). Visual object tracking using adaptive correlation filters. 2010 IEEE Computer Society Conference on Computer Vision and Pattern Recognition, pp. 2544–2550.
47. Felzenszwalb, P.F., Girshick, R.B., McAllester, D., and Ramanan, D. (2010). Object detection with discriminatively trained part-based models. *IEEE Trans. Pattern Anal. Mach. Intell.* **32**, 1627–1645.
48. Dollár, P. (2013). *Piotr's Computer Vision Matlab Toolbox (PMT)*. <https://github.com/pdollar/toolbox>.
49. Rauch, H.E., Striebel, C., and Tung, F. (1965). Maximum likelihood estimates of linear dynamic systems. *AIAA J.* **3**, 1445–1450.
50. Ahrens, M.B., Li, J.M., Orger, M.B., Robson, D.N., Schier, A.F., Engert, F., and Portugues, R. (2012). Brain-wide neuronal dynamics during motor adaptation in zebrafish. *Nature* **485**, 471–477.

STAR★METHODS

KEY RESOURCES TABLE

REAGENT or RESOURCE	SOURCE	IDENTIFIER
Experimental Models: Organisms/Strains		
Zebrafish: Tg(<i>elavl3:GCaMP6s</i>)	[44]	RRID: ZFIN Tg insertion jf5Tg
Zebrafish: wild-type Tupfel long-fin	N/A	ZFIN ID: ZDB-GENO-990623-2
Software and Algorithms		
MATLAB (data analysis)	Mathworks	https://www.mathworks.com/products/matlab.html
StreamPix 7	Norpix	https://www.norpix.com/products/streampix/streampix.php
Psychophysics toolbox	N/A	http://psychtoolbox.org/
Zen Black 2012 Service Pack 2 (Image acquisition)	Carl Zeiss Pty Ltd	http://www.zeiss.com

RESOURCE AVAILABILITY

Lead Contact

Further information and requests for resources should be directed to and will be fulfilled by the Lead Contact, Geoffrey J. Goodhill (g.goodhill@uq.edu.au).

Materials Availability

This study did not generate new unique reagents.

Data and Code Availability

The behavioral data and related code are available at https://github.com/GoodhillLab/Zebrafish_hunting_behavior. The neuroimaging dataset is complex, and is also intertwined with a different imaging dataset from the same set of fish which forms the basis for a different forthcoming publication. We are currently working to put the entire dataset into a form useful for other researchers, and it will be released as soon as possible. For specific requests in the meantime please contact the Lead Contact.

EXPERIMENTAL MODEL AND SUBJECT DETAILS

Zebrafish

Nacre zebrafish (*Danio rerio*) embryos expressing *elavl3:H2B-GCaMP6s* [44] were collected and raised according to established procedures [45] and kept under a 14/10 h on/off light cycle. Larvae were fed live rotifers (*Brachionus plicatilis*) daily from 5 dpf. All procedures were performed with approval from The University of Queensland Animal Ethics Committee.

METHOD DETAILS

Hunting behavior assay

89 individual fish larvae (34, 22, 33 fish aged 5, 8–9, 13–15 dpf respectively) were placed (singly) into a clear bottom recording chamber (diameter: 20 mm; depth: 2.5 mm; CoverWell Imaging Chambers. Catalogue number 635031, Grace Biolabs), containing E3 embryo medium with fluid depth 2.5 mm and 30–50 *Paramecia* (*Paramecium caudatum*). Chambers were placed on a heating plate heated to 28.5°C (Fryer), illuminated from the bottom with an LED ring (LDR2-100SW2-LA, Creating Customer Satisfaction (CCS) Inc., Kyoto, Japan) and imaged with a stereoscope (Zeiss StereoDiscovery V8, 0.5X objective lens) equipped with a CMOS camera (Grasshopper GS3-U3-23S6M-C, Point Grey), at 100 fps. To achieve a faster imaging rate for a small number of fish, chambers were illuminated from the bottom with an infrared LED ring (850 nm, LDR2-100IR2-850-LA powered by PD3-3024-3-PI, CCS), from the top with a white light ring (LDR2-100SW2-LA, CCS Inc., Kyoto, Japan) and imaged with a CMOS camera (Mikrotron 4CXP, Mikrotron) at 300 fps ($n = 7$) or 500 fps ($n = 13$). A small set of chambers ($n = 12$, 16 fish age 5 and 9 dpf respectively) were imaged without a heating plate, but no statistical differences in hunting behavior characteristics (duration, detection angle, number of bouts, hit ratio) were observed except for a decrease in hunting event rate in the non-heated plates (t test). Overall a total of 2569 hunting events were recorded.

Imaging hunting behavior of individuals over development

To track the development of hunting behavior for individual fish, GCaMP6s larvae were individually housed from 1 dpf in dishes with age-matched non-GCaMP fish (to allow the target individual to be identified). We then used the assay described above to image hunting behavior of the GCaMP6s larvae at both 5 and 13 dpf.

Analysis of hunting behavior movies

Movies were visually inspected and measures were extracted using ImageJ (Grasshopper movies) or StreamPix (Mikrotron movies). Results for 12% of the movies (10/86) were cross validated between 2–4 observers to ensure measurement consistency and minimize inter-examiner variability. The start and end of each hunting event were determined by eye convergence [23]. For each fish and each event we extracted the following measures characterizing event properties. Event duration was defined as the time between eye convergence and divergence. Detection angle was defined as the angle between the larva's head direction and the vector defined by the point between the eyes on the midline and the *Paramecium* (Figure 1F). The *Paramecium* of interest was defined as the nearest *Paramecium* toward which the fish performed the first turn movement. We further measured the post-bout angle between the larva and the *Paramecium* after the first bout, number of bouts between the start and end of the event, and hunting hit ratio. To evaluate hit ratio we labeled every event using three labels (hit, miss and abort). In an 'abort' event, the larva chases but never lunges toward the prey. In a 'miss' event, the larva chases, inaccurately lunges toward the prey, and therefore misses the *Paramecium*. In a 'hit' event the larva chases, accurately strikes and captures the *Paramecium* of interest. This label also includes events where the *Paramecium* is caught by the larva and immediately released, since the prey was accurately localized in these cases. Hit ratio was calculated as the ratio of hit events out of all hunting events (hit, miss and abort) for a given fish. For each measure we obtained an average over all events per fish, and changes in the statistics of these averages over development were examined.

To assist in the extraction of behavioral measures we used custom image processing software written in MATLAB to analyze 25 of the movies. Movies were first pre-processed to create a foreground mask for the fish and the *Paramecium*, allowing us to remove background information in each frame. A Gaussian background model of each pixel was fitted over the set of every tenth frame of the movie. A pixel was classified as foreground in a given frame if its intensity was lower than 3 standard deviations from the pixel's mean intensity or higher than 3 standard deviations from its mean. To obtain an initial estimate of the position of the fish in each frame, we used connected components analysis on the foreground mask to extract the largest component, which was a mask of the fish. We then cropped a 128×128 pixel tracking window around the center of mass of the fish mask to reduce computational load for the next stage of the processing pipeline.

To compute the position and heading angle of each fish we tracked a point on the center of the swim bladder and the midpoint between the eyes using a custom correlation filter approach based on the Minimum Output Sum of Squared Error (MOSSE) filter [46]. To make tracking more robust, we trained a set of MOSSE filters using different features from the image. These features included the pixel intensity and an extended set of 31 histogram of gradients (HOG) features described in [47] computed using *Piotr's Image & Video MATLAB Toolbox* [48]. To train the MOSSE filters we: (i) selected a set of 10 training frames; (ii) centered and rotated the fish to 0 degrees in each frame; (iii) cropped a 128×128 pixel window around the fish; (iv) extracted the features to produce a set of training patches per feature; and (v) trained the MOSSE filter for each feature on its respective set of training patches. To enable tracking of the fish at different orientations, we repeated the filter training process for 72 evenly spaced rotations of the training patches over 360 degrees to create a rotated filter stack for each feature. To track the desired point on the fish in a given frame, we correlated the cropped tracking window with the rotated filter stack for each feature. We then computed the mean correlation over the set of features and identified the rotation that results in the maximally correlated pixel. This pixel was taken to be the location of the desired tracking point. The tracked trajectories for the eye midpoint and swim bladder were both smoothed using a Kalman Smoother (Rauch–Tung–Striebel algorithm) [49] with Newtonian mechanics and constant acceleration.

To detect bouts we used the kinematics of the midline of the tail. The tail midline was estimated by performing a morphological thinning operation on the fish mask using MATLAB's *bwmorph* function and pruning the resulting skeleton by finding the geodesic path between the swim bladder and the tip of the tail in the corresponding connected components graph. The midline was then smoothed in both *x* and *y* directions using a moving mean. A 1-dimensional constant velocity Kalman smoother was used to estimate the length of the tail which varies with the pitch of the fish. Ten evenly spaced points were then extracted by linearly interpolating along 95% of the length of the midline starting at the head end. We discarded the most posterior 5% of the tail because the relative illumination of this segment of the tail was low, resulting in noise. We then computed the angle θ_i between tail segments between the *i*-th and *i*+1-th tail point for *i* = 1, 2, ..., 9. Subsequently we computed the mean of the angular velocity $\bar{\omega}$ for the 4 most posterior tail segments:

$$\bar{\omega} = \frac{1}{4} \sum_{i=6}^9 \frac{d\theta_i}{dt}. \quad (\text{Equation 1})$$

We then took the absolute value $|\bar{\omega}|$ and applied a moving mean of 5 samples to smooth. Bouts were detected by applying a threshold which was selected manually and verified by visual inspection. We applied additional constraints that bouts must be at least 50 ms long, and adjacent bouts must be separated by more than 20 ms else they were merged and treated as a single bout.

To track the location of *Paramecia* in each frame, the foreground mask was first filtered to retain connected components with area between 9 and 196 pixels. The centroids of each component were treated as detected locations of *Paramecia*. Each detected centroid was assigned to an existing track from the previous frame based on the minimum Euclidean distance between the detection and the existing track. If no suitable track existed then a new track was created. A constant velocity Kalman filter was used to track prey through short periods of occlusion such as when they swam under the fish.

Each hunting event was manually inspected to record the beginning and end of the event, identify the *Paramecium* being hunted, and determine feeding event score. Using this information in conjunction with the fish and prey tracking enabled the computation of

the behavioral measures. Results were manually validated and corrected as necessary using annotated output videos produced by the software.

To investigate developmental changes in the angle that the fish turns toward its prey in the first bout of a hunting event, we fit the following multiple regression model to the feeding assay data:

$$\theta_{\text{postbout}} = \beta_0 + \beta_1 \theta_{\text{detection}} + \beta_2 \text{age} + \beta_3 \theta_{\text{detection}} \text{age} + \varepsilon$$

where θ_{postbout} is the prey angle after the first bout (measured in degrees), $\theta_{\text{detection}}$ is the prey angle on detection, age is the fish age (measured in dpf), $\{\beta_0, \dots, \beta_3\}$ are the model coefficients and ε is the error term.

2-photon calcium imaging

Zebrafish larvae were embedded in 2.5% low-melting point agarose, positioned at the center of a 35 mm diameter plastic Petri dish and overlaid with E3 embryo medium. Time-lapse 2-photon images were acquired at the Queensland Brain Institute's Advanced Microscopy Facility using a Zeiss LSM 710 inverted 2-photon microscope. A custom-made inverter tube composed of a pair of beam-steering mirrors and two identical 60 mm focal length lenses arranged in a 4f configuration was used to allow imaging with a 40X/1.0 NA water-dipping objective (Zeiss) in an upright configuration. Samples were excited via a Spectra-Physics Mai Tai DeepSee Ti:Sapphire laser (Spectra-Physics) at an excitation wavelength of 940 nm. Calcium imaging was performed at depths of 55, 70, 85, 100 μm from the dorsal surface of the tectal midline, where each plane was recorded from a different fish. Laser power at the sample plane ranged between 12 to 20 mW. Emitted light was bandpass filtered (500–550 nm) and detected with a nondescanned detector. Time-lapse images (416 \times 300 pixels) were obtained at 2.2 Hz. To improve stability of the recording, chambers were left to settle prior to imaging for 3 h.

Visual stimulation

Visual stimuli were projected onto white diffusion paper placed around the wall of the Petri dish, using a pico-projector (PK320 Optoma, USA), covering a horizontal field of view of 174°. To prevent stimulus reflection, the opposite side of the dish was covered with low-reflection black paper. To avoid interference of the projected image with the signal collected by the detector, a red long-pass filter (Zeiss LP590 filter) was placed in front of the projector. Larvae were aligned with one eye facing the projected side of the dish and body axis at right angles to the projector direction. Visual stimuli were generated using custom software based on MATLAB (MathWorks) and Psychophysics Toolbox (<http://psychtoolbox.org>).

To map the visual field at 70 μm (Figures 2–4), each trial consisted of 6 degree diameter black spots at nine different positions from 45° to 165° with 15° intervals, with their order set to maximize spatial separation within a trial (45°, 120°, 60°, 135°, 75°, 150°, 90°, 165°, 105°). 0° was defined as the direction of the larvae's body axis. Spots were presented for 1 s each, followed by 20 s of blank screen. We projected 20 consecutive trials of nine spots with 25 s of inter-trial interval. The entire experiment lasted 96.6 min (the first 35 min was spontaneous activity in the dark, which is not considered here). A protocol composed of 20 trials of 11 spots (15°–165° with 15° interval) was used in one fish, and a protocol with 5 trials of 11 spots and 20 repetitions of 8 spots (60°–165° with 15° interval) was used in 12 fish. Edits to the experimental protocol were made since anterior responses were very weak early in development and we had no *a priori* knowledge this was a developmental effect.

To map the visual field at 100 μm (Figure 3C–H), we used 10 trials of 11 spots (15°–165° with 15° interval) and 25 s of inter-trial interval, $n = 6$, 5 of 5 and 13–15 respectively. To map tectal responses in different tectal depths over development (Figure 3A–B), we presented 4 trials of 4 spots (15°–60° with 15° interval) and recorded tectal activity at 55, 70, 85, 100 μm from the dorsal surface of the tectal midline at 5 and at 8–9 dpf.

Automatic cell detection

Alignment of data stacks and cell detection procedure were performed as in [18]. All fluorescence data stacks were corrected for x-y drifts using custom MATLAB software based on rigid image registration algorithm. The software automatically detected the set of pixels of each active cell and searched for pixels that showed changes in brightness across frames, resulting in an activity heatmap of all the active regions across frames [50]. This activity map was then segmented into regions using a watershed algorithm, with a movie-specific threshold that was similar across fish. Within each segmented region, we computed correlation coefficients of all pixels in the region with the mean of the most active pixel and its eight neighboring pixels. Correlation coefficients showed a bimodal distribution; one peak of highly correlated pixels representing pixels of the cell within the region, and a second peak of relatively low correlation coefficients representing nearby pixels within the region which were not part of the cell. Using a Gaussian mixture model, we found the threshold correlation which differentiated between pixels likely to form the active cell and neighboring pixels that were not part of the cell. We also required that each detected active area covered at least 26 pixels (5.5 μm^2). The software allowed visual inspection and modification of the parameter values where needed. All pixels assigned to a given cell were averaged to give a raw fluorescence trace over time. Raw calcium signals for each cell, $F(t)$, were then converted to represent changes from baseline level, $\Delta F/F(t)$ defined as $(F(t) - F_0(t))/F_0(t)$. The time varying baseline fluorescence, $F_0(t)$, for each cell was a smoothed curve fitted to the lower 20% of the points. $F_0(t)$ was the minimum of the smoothed fluorescence trace in a 3 s window centered at t .

Tuning curves

For each neuron we calculated the mean amplitude across frames 4–7 post stimulus presentation. These amplitudes were then averaged per stimulus, providing for each neuron a curve of mean amplitude in response to all presented stimuli. Cubic spline interpolation was used to estimate the amplitude values between the presented stimuli at 5° intervals. This interpolated curve of amplitudes was fitted with a Gaussian with baseline offset. Fit starting points used the mean as the stimulus value eliciting response peak amplitude, and the initial value for standard deviation was varied from low to high values. The fitted curve which provided the highest goodness of fit (adjusted r^2) was selected as the fit of the tuning curve. Neurons with goodness of fit greater than 0.7 were deemed to be selective neurons and included in further analysis.

Decoding stimulus identity

For the results shown in Figure 4 we used linear discriminant analysis to decode stimulus identity. The algorithm received as an input a set of population response vectors of all selective neurons ($20 \times 9 = 180$ vectors representing response averaged over frames between 1.5 s and 3.5 s post stimulus presentation) and their respective stimulus labels (i.e., the stimulus evoking each population response vector). Neurons which were active only spontaneously and were not selective to the stimuli were not included in the population response vectors. The algorithm output the linear discriminant coefficients for the population for the nine different stimuli. Decoder classification coefficients were calculated from a training set separate from the test set to be decoded, using a leave-one-out strategy, in which a single population response vector was decoded using the statistics calculated on the basis of all presentations other than the test vector. Given a test population response, scores were calculated for each stimulus and the respective stimulus identity probability. The test population response was classified as the most probable stimulus. Overall decoding performance per fish was defined as the proportion of population responses classified correctly out of the 180 responses tested.

In addition to a linear decoder we used several other decoders (Figure S3A). The first was a topography-based decoder which relies on the Centre of Mass (CoM) of tectal responses as described in [21]. By averaging the CoM of all the responses in the training set evoked by a given stimulus, we obtained a set of CoMs each corresponding to a particular stimulus. We then calculated the CoM of a given test response, and assigned it to the stimulus with the nearest CoM. The second was a Maximum Likelihood decoder (ML) as described in [21], where decoding the population response consisted of searching for the stimulus, which had the highest probability of evoking a given population response. Next we then used three decoders taking into account only mean of the responses (M), or the mean and variance of the responses (M+V), and lastly the mean and the full covariance matrix (M+Cov). For the decoder based on mean responses, population responses in the training set were averaged per stimulus, resulting in a mean population response representing each stimulus. We then calculated the Euclidean distance between the test response and any of the mean responses, and assigned the test response to the stimulus whose corresponding mean response was closest. For the decoders based on either mean and variance or the mean and entire covariance matrix of the responses, we first calculated the covariance matrix. Similar to [4], the stimulus independent covariance matrix was computed as the mean of the covariance matrices for the individual stimuli

$$Cov = \frac{1}{N_t N_s} \sum_{i=1}^{N_s} \sum_{t=1}^{N_t} (r_{i,t} - \bar{r}_i) (r_{i,t} - \bar{r}_i)^T$$

Where N_t is the number of trials, N_s is the number of stimuli and $r_{i,t}$ is the population response to stimulus i in trial t . The covariance matrix was used in two ways: as a whole for the M+Cov case, or where all off diagonal values were zeroed (M+V). Inspired by the discriminability measure introduced in [4], we evaluated the multivariate normal distributions centered at the mean responses to the different stimuli at the test response. These densities were normalized so that their value was 1 at the center. The stimulus providing the highest value at the test response was selected as the decoded stimulus.

Information theory analysis

We binarized the raster of the neurons based on a threshold of mean amplitude plus two standard deviations for each neuron [18]. We then estimated the probability that a neuron was active in response to a particular stimulus s , $P(r = 1|s)$, in the frames between 1.5 s and 3.5 s after any of the presentations of stimulus s . The probability of the stimulus, $P(s)$, was uniform by experimental design. Mutual information between the activity of any particular neuron and the stimuli was then computed as

$$-\sum_{r=0,1} \sum_s P(r|s)P(s) \log_2 \sum_{s'} P(r|s')P(s') + \sum_{r=0,1} \sum_s P(r|s)P(s) \log_2 P(r|s),$$

where the first term is the entropy of that neuron. Besides the complete set of stimuli we sometimes considered the mutual information and entropy for different stimulus subsets. In these cases the stimulus sum was restricted to only those stimuli and $P(s)$ was appropriately normalized.

The mutual information is trivially bounded by the smallest of either the stimulus entropy or response entropy. In our case, where the stimuli were approximately uniformly distributed on subsets of at least 3 stimuli, the stimulus entropy always exceeded the response entropy so that mutual information was bound by the latter. We obtained the average distribution of mutual information and entropy along the anterior-posterior axis using a moving average approach. For every point along the axis we computed the average distribution at this point as the mean across the neurons that were projected into a small interval of 0.15 times the length of the AP axis around this point.

Modeling information theory results

We considered a stimulus variable S drawn from a discrete set of stimulus values where each value corresponds to a stimulus azimuthal angle $\{\Theta_s\}_s$. We modeled the activity X^θ of a single neuron tuned to angle θ as a Bernoulli variable with a response parameter modulated by the stimulus that is presented, i.e., $X^\theta | S \sim \text{Ber}(p_s^\theta)$, where $p_s^\theta = p_0 + \Delta p \cdot \rho\left(\frac{\theta - \Theta_s}{\sigma}\right)$ and ρ is an unnormalized Gaussian function centered at 0 with variance of 1, so that the width of the neuron's receptive field is parameterised by σ and its preferred azimuthal angle is θ . (Figure S5B).

The mutual information between the stimulus variable and the activity of each neuron is

$$\text{MI}(S; X^\theta) = h(\mathbb{E}[p_s^\theta]) - \mathbb{E}[h(p_s^\theta)],$$

where $h(p) = -p \log_2 p - (1-p) \log_2 (1-p)$ is the Bernoulli entropy.

Imposing beta distributions on the response probabilities, $(p_s^\theta)_s$, with shape parameters α and β we can explicitly compute the mutual information as

$$\text{MI}(S; X^\theta) = h\left(\frac{\alpha}{\alpha + \beta}\right) - \frac{1}{\ln 2} \left(\psi(\alpha + \beta + 1) - \frac{\alpha}{\alpha + \beta} \psi(\alpha + 1) - \frac{\beta}{\alpha + \beta} \psi(\beta + 1) \right)$$

where ψ denotes the digamma function. Since the shape parameters can be uniquely expressed in terms of the expectation and mean of the corresponding distribution,

$$\alpha = \mathbb{E}[\text{Beta}(\alpha, \beta)] \nu \quad \text{where } \nu = \frac{\mathbb{E}[\text{Beta}(\alpha, \beta)](1 - \mathbb{E}[\text{Beta}(\alpha, \beta)])}{\text{Var}[\text{Beta}(\alpha, \beta)]} - 1,$$

$$\beta = (1 - \mathbb{E}[\text{Beta}(\alpha, \beta)]) \nu$$

this yields an explicit expression of the mutual information in the Bernoulli model with beta distributed Bernoulli parameters. This is particularly instructive when considering the possible values of mutual information, parameterised in terms of expectation and variance of the response probabilities (Figures S5C and S5D). In order for a neuron to express large values of mutual information, the variance has to be large and consequently the expectation close to 1/2: for any random variable Q taking values in the unit interval, $\text{Var}[Q] \leq \mathbb{E}[Q](1 - \mathbb{E}[Q])$.

The dependence of mutual information on the variance can also be seen directly, if we express p_s^θ in terms of deviations from its mean and assume that these deviations are sufficiently small. The mutual information can then be expanded around $\mathbb{E}[p_s^\theta]$ to yield

$$\text{MI}(S; X^\theta) \approx \frac{1}{2 \ln 2} \frac{\text{Var}[p_s^\theta]}{\mathbb{E}[p_s^\theta](1 - \mathbb{E}[p_s^\theta])}$$

where errors to this approximation are cubic in the deviations from the mean.

We considered a population of neurons that are modeled by such a Bernoulli model and placed along a sensory axis representing the visual field, parameterised by angles from 0° to 180° . In the case of a regular map, the position of neurons along this axis corresponds to the center of their receptive fields (their preferred azimuthal angle). To introduce irregularity into this sensory map we kept the position of the neurons constant but shifted the receptive field centers by adding Gaussian noise with mean 0 and standard deviation of 9° . We matched the parameters of the neuron model closely to the experimental data ($p_0 = 0.05$, $\Delta p = 0.85$) with three stimuli around the center of the visual field (75° , 90° and 105°) and considered a population of 200 neurons. In order to describe a continuous mutual information distribution along the sensory axis we computed a moving average with sliding window width of 9° .

QUANTIFICATION AND STATISTICAL ANALYSIS

For datasets which passed the Anderson-Darling goodness-of-fit of normal distribution we used a two-sample or paired t tests as appropriate. For datasets which did not pass the normality test we used a Wilcoxon rank sum test for independent samples. When multiple testing was performed we used Bonferroni multiple comparison correction to control for the number of false positives.

Current Biology, Volume 30

Supplemental Information

Behavioral Signatures of a Developing Neural Code

Lilach Avitan, Zac Pujic, Jan Mölter, Michael McCullough, Shuyu Zhu, Biao Sun, Ann-Elin Myhre, and Geoffrey J. Goodhill

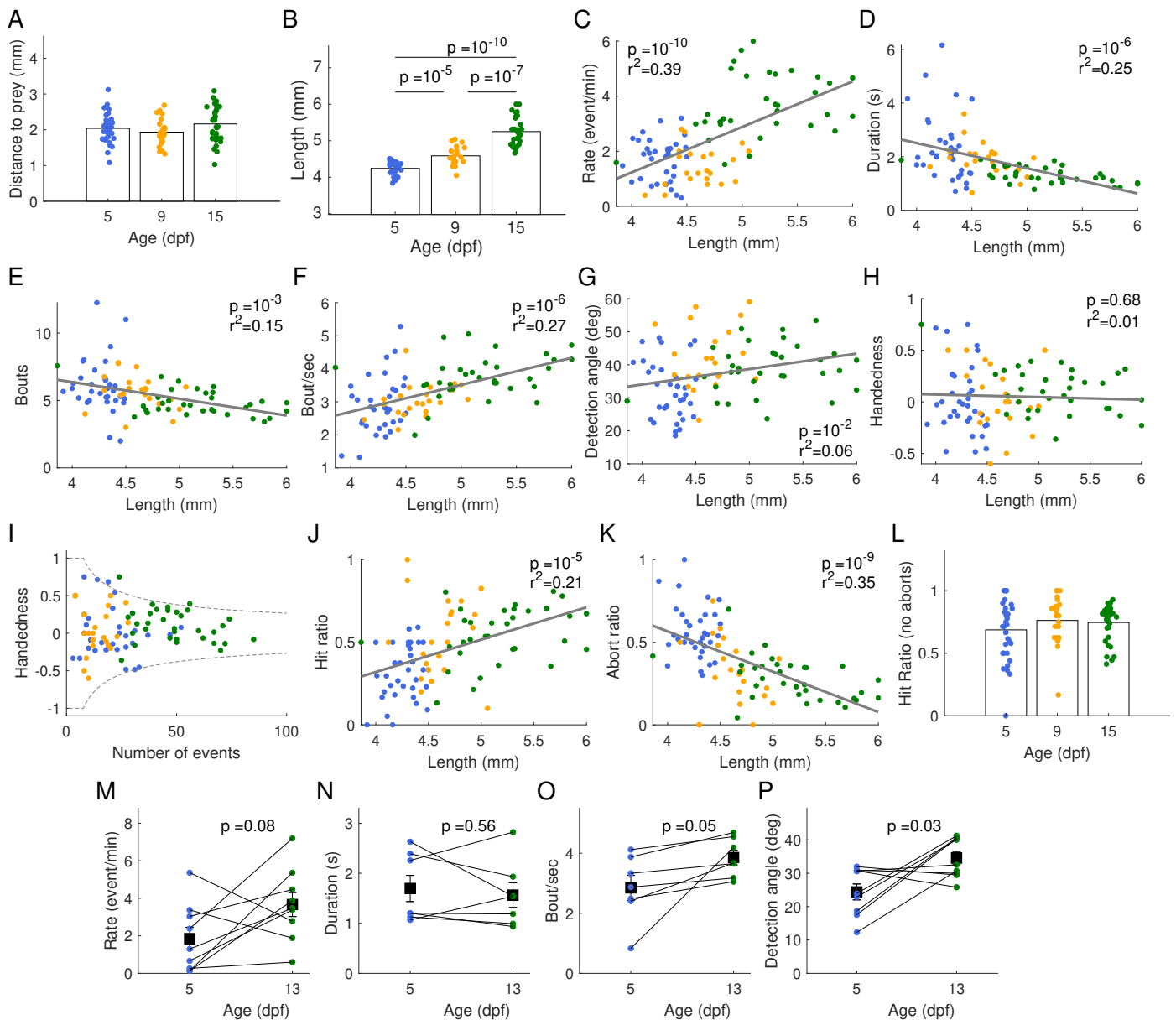


Figure S1: Improvement in hunting measures with length and within individuals, Related to Figure 1. A: Distance to detected prey at the onset of the event did not change over development. B: Fish length increased over development, though with a substantial overlap between age groups. C: Event rate increased as a function of length (colours indicate age as shown in panel A). D: Event duration decreased as a function of length. E: Number of bouts decreased as a function of length. F: Bout rate increased as a function of length. G: *Paramecium* detection angle increased as a function of length. H: Handedness did not depend on length. I: Handedness decreased as a function of number of hunting events recorded. Handedness index mostly fell within the region expected under the null hypothesis that detection events are independent and uniform Bernoulli instances with a probability of at least 99% (marked by the grey lines), indicating no lateralization in *Paramecia* detection. J: Hit ratio increased with length. K: Abort ratio decreased with length. L: Ratio of hits compared to hits plus misses over development showed a slight trend but was not significantly different. M–P show results for 9 fish that were behaviorally assessed at both 5 and 13 dpf. M: Event rate showed an increasing trend. N: Hunting duration was not different for this small number of samples. O: Bout rate increased over development. P: *Paramecia* detection angle increased over development.

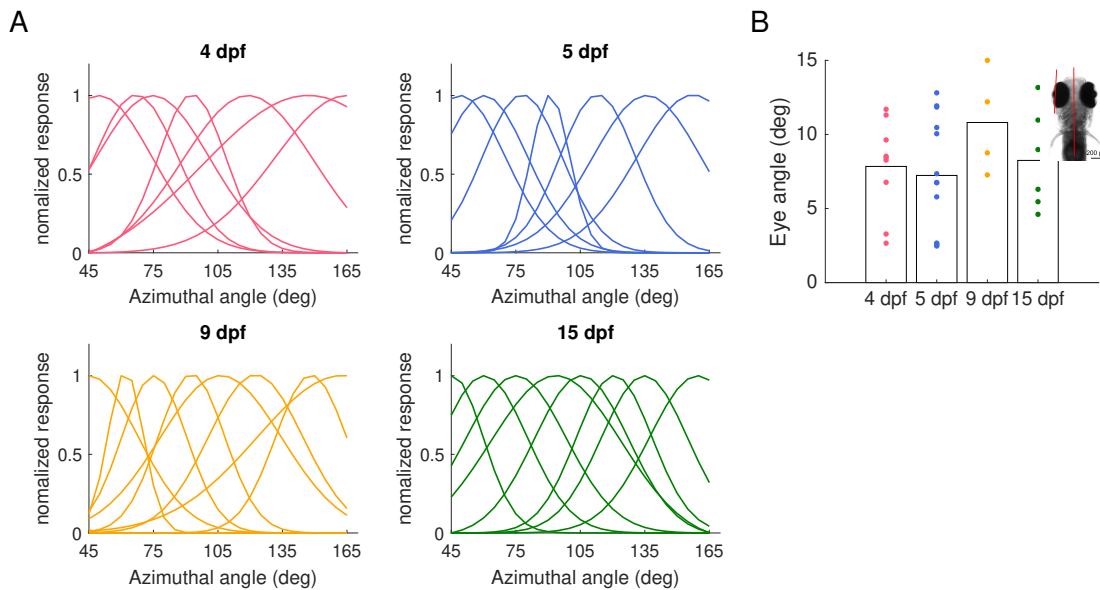


Figure S2: Further investigation of tectal responses, Related Figure 2. A: Normalized fitted tuning curves for example 4, 5, 9, and 15 dpf fish at 70 μm depth demonstrating tuning coverage of the visual field. Tuning curves were normalized so that their value was 1 at their peak. B: Inset: The head of the fish was imaged at the end of every 2-photon imaging session and the angle between the eye and the midline was calculated. No difference over development was observed in this angle ($p = 0.39$, one-way ANOVA).

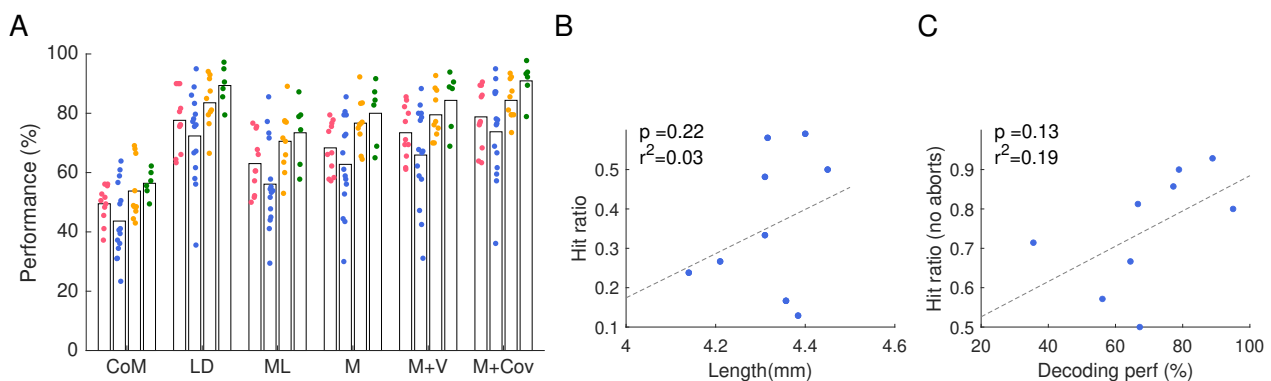


Figure S3: Further analysis of decoding performance at 70 μm depth, Related to Figure 4. A: Decoding performance improved over development. Decoders used were: a topography-based decoder which uses the response centre of mass (CoM), a linear decoder (LD), a maximum likelihood decoder (ML), a decoder which is based on population mean response (M), a decoder based on response mean and variance (M+V), and a decoder based on mean, variance and covariance (M+Cov). Similar to previous reports (Avitan et al. 2016), the ML decoder outperformed the CoM decoder. No difference in performance was found between the decoder based on mean response and the decoder based on mean and variance ($p = 0.55$, one-way ANOVA). No difference in performance was found between M+V decoder and M+Cov decoder ($p = 0.09$, one-way ANOVA), however an improvement in decoding performance was found between M and M+Cov decoder ($p = 10^{-2}$, one-way ANOVA). B: There was no correlation ($r^2 = 0.03$) between hunting hit ratio and fish length. C: There was a small-moderate correlation ($r^2 = 0.19$) between decoding performance and hunting hit ratio where abort events are excluded.

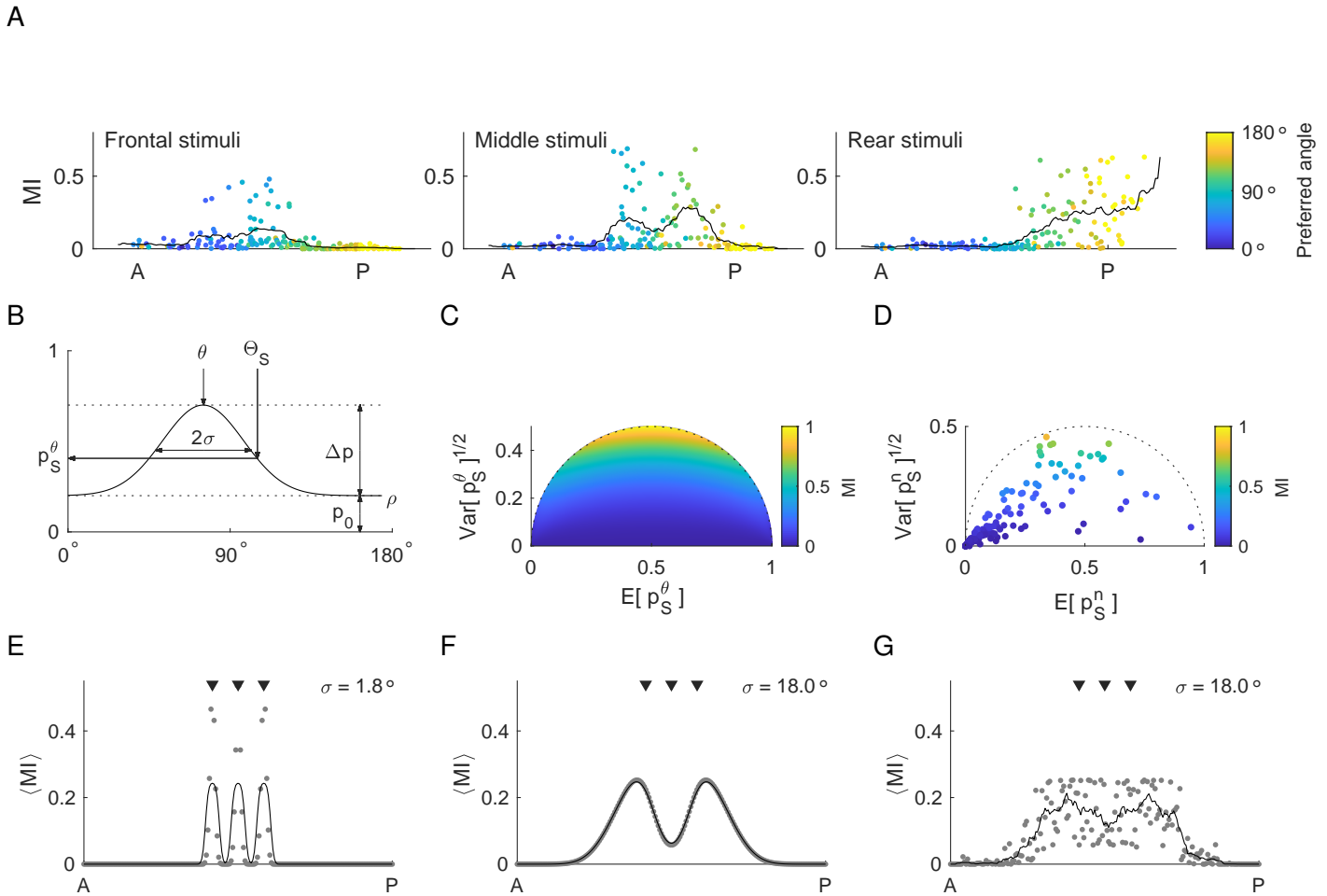


Figure S4: The distribution of mutual information over the AP axis at 70 μm depth appears bimodal for wide receptive fields, Related to Figure 5. A: Distribution of mutual information between tectal neural response and the frontal, middle and rear stimulus sets along the AP axis in an example fish. Variations of bimodal distributions were apparent in all fish. Mutual information between neural activity and the middle stimulus set appears bimodal. Neurons' preferred azimuthal angle is color coded. B: The response probability p_S^θ for a neuron in the Bernoulli model with a constant offset p_0 and a term to modulate its response $\Delta p \rho \left(\frac{\theta - \Theta_S}{\sigma} \right)$. The neuron has a Gaussian receptive field function ρ of width σ and a preferred azimuthal angle θ and the stimulus angle is Θ_S . C: Mutual information as a function of expectation and variance of beta- distributed response probabilities. Large values of mutual information can only be achieved for response probabilities that have a large variance. D: Mutual information as a function of expectation and variance of response probabilities estimated from tectal neural activity for the set of middle stimuli. Only very few neurons show high enough variance in their response probabilities to reach large values of mutual information. E–G: Simulated mutual information distribution, for a population of 200 neurons. The distribution is computed as a moving average of mutual information of the different neighbouring neurons. The triangles indicate the position of the stimuli at 75°, 90° and 105°. For narrow receptive fields and a regular sensory map, the distribution appears locally unimodal around the stimulus positions (E). For wider receptive fields which match experimental data and in the case of a regular sensory map (F) as well as an irregular sensory map (G), the mutual information appear globally bimodal due to overlapping receptive fields to the different stimuli.